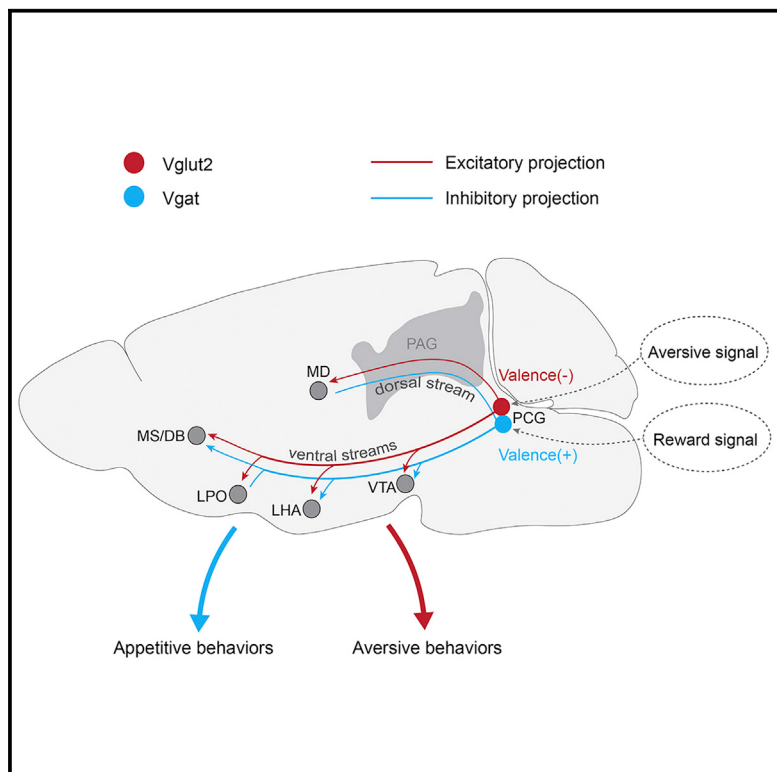


# Glutamatergic and GABAergic neurons in pontine central gray mediate opposing valence-specific behaviors through a global network

## Graphical abstract



## Authors

Cuiyu Xiao, Jinxing Wei,  
Guang-wei Zhang, ...,  
Ian R. Wickersham, Huizhong W. Tao,  
Li I. Zhang

## Correspondence

htao@usc.edu (H.W.T.),  
liizhang@usc.edu (L.I.Z.)

## In brief

Xiao et al. find that pontine central gray (PCG) contributes to encoding positive and negative valences through the activity of its GABAergic and glutamatergic neurons, respectively, which mediate sensory-induced reward- and aversion-related behaviors. Thus, PCG may serve as a critical hub for the bottom-up processing of sensory valence preceding the limbic system.

## Highlights

- PCG glutamate and GABA neurons encode negative and positive valence, respectively
- These neurons mediate aversion and appetitive behaviors, respectively
- Input-output organizations of PCG glutamate and GABA neurons are characterized
- PCG relays valence information into a globally distributed network



## Article

# Glutamatergic and GABAergic neurons in pontine central gray mediate opposing valence-specific behaviors through a global network

Cuiyu Xiao,<sup>1,5</sup> Jinxing Wei,<sup>1,5</sup> Guang-wei Zhang,<sup>1</sup> Can Tao,<sup>1</sup> Junxiang J. Huang,<sup>1,2</sup> Li Shen,<sup>1</sup> Ian R. Wickersham,<sup>4</sup> Huizhong W. Tao,<sup>1,3,\*</sup> and Li I. Zhang<sup>1,3,6,\*</sup>

<sup>1</sup>Zilkha Neurogenetic Institute, Department of Physiology and Neuroscience, Keck School of Medicine, University of Southern California, Los Angeles, CA 90033, USA

<sup>2</sup>Graduate Program in Biological and Biomedical Sciences, University of Southern California, Los Angeles, CA 90089, USA

<sup>3</sup>Center for Neural Circuits and Sensory Processing Disorders, Keck School of Medicine, University of Southern California, Los Angeles, CA 90033, USA

<sup>4</sup>McGovern Institute for Brain Research, Massachusetts Institute of Technology, Cambridge, MA 02139, USA

<sup>5</sup>These authors contributed equally

<sup>6</sup>Lead contact

\*Correspondence: htao@usc.edu (H.W.T.), liizhang@usc.edu (L.I.Z.)

<https://doi.org/10.1016/j.neuron.2023.02.012>

## SUMMARY

Extracting the valence of environmental cues is critical for animals' survival. How valence in sensory signals is encoded and transformed to produce distinct behavioral responses remains not well understood. Here, we report that the mouse pontine central gray (PCG) contributes to encoding both negative and positive valences. PCG glutamatergic neurons were activated selectively by aversive, but not reward, stimuli, whereas its GABAergic neurons were preferentially activated by reward signals. The optogenetic activation of these two populations resulted in avoidance and preference behavior, respectively, and was sufficient to induce conditioned place aversion/preference. Suppression of them reduced sensory-induced aversive and appetitive behaviors, respectively. These two functionally opponent populations, receiving a broad range of inputs from overlapping yet distinct sources, broadcast valence-specific information to a distributed brain network with distinguishable downstream effectors. Thus, PCG serves as a critical hub to process positive and negative valences of incoming sensory signals and drive valence-specific behaviors with distinct circuits.

## INTRODUCTION

In natural environments, animals are bombarded with barrages of sensory information. Yet, they are able to filter out unimportant information and rapidly respond to the dynamic surroundings in an adaptive manner. The valence of environmental cues is defined by their associated positive or negative outcomes.<sup>1–3</sup> Detecting and discriminating the valence of external signals are thus essential for animals' survival and well-being. Negative valence signals usually result in avoidance/aversive behaviors, whereas positive valence signals result in approach/appetitive behaviors.<sup>4–7</sup> Although abundant previous studies have been focused on how different brain structures and cell types are involved in aversion- or reward-related emotional processing,<sup>8–18</sup> how values of valence are extracted from incoming sensory signals and represented by neurons along the sensory processing pathways remains largely unclear.

Valence coding neurons are those exhibiting differential responses to cues associated with reward and threat/punishment,

independent of modality.<sup>16–18</sup> Previous studies searching for valence coding neurons have identified a great number of brain regions relevant to emotional/motivational processing. These regions include the amygdala, hippocampus, prefrontal cortex, striatum, lateral hypothalamus, habenula, and various neuromodulatory systems,<sup>11,14–30</sup> suggesting that the valence processing framework may involve a large distributed brain network. How valence is transformed from sensory signals, however, is unknown. As structures outside the traditionally recognized limbic system and related circuitry have not been well studied under the context of reward/punishment, it remains possible that even at an early sensory information processing stage preceding the classic limbic system, valence information has already been processed by specific neuronal populations.

In humans, previous studies have suggested that the pons could work conjunctively with the distributed corticolimbic system to shape an individual's affective states,<sup>31,32</sup> especially for negative affective states.<sup>33</sup> In particular, the dorsal pons has been found activated during recalled experiences of negative



emotion.<sup>34</sup> These findings raise a possibility that specific structures in the dorsal pons might be involved in valence and emotional processing. Here, we directly targeted a salient structure located in the dorsal pons, the pontine central gray (PCG). The PCG is a distinct cell group in caudoventral regions of the pontine periventricular gray, adjacent to the caudal dorsal tegmental nucleus (DTN). Previous studies in related areas have mostly been focused on sleep-wake regulation,<sup>35,36</sup> as well as sensory relay.<sup>37–40</sup> The anatomical and functional roles of PCG in valence processing remain largely unclear.

By combining *in vivo* electrophysiology and fiber photometry recording, we found that two genetically defined neuronal populations in PCG encoded opposite valences. The glutamatergic neurons were specifically activated by aversive, but not reward, sensory inputs, while the GABAergic neurons responded preferentially to reward signals. Optogenetic activation of the glutamatergic and GABAergic neurons acutely resulted in avoidance and preference behaviors, respectively, and was sufficient to induce conditioned place aversion (CPA) or preference (CPP). On the other hand, optogenetic suppression of these neurons attenuated sensory-induced aversion and reward-related behaviors. Using cell-type-specific anatomical tracing and projection-specific manipulations, we found that the two PCG neuronal populations had largely overlapping yet distinguishable input-output patterns. They receive the most prominent input from the pontine reticular nucleus (PRN) and orbital frontal cortex (OFC), respectively. Through distinct output projections, they relay the valence-specific information into a distributed brain network known to be involved in motivational processing. Our results suggest that PCG, although at a relatively early stage of sensory processing, can already distinguish sensory valences through the activity of two functionally opponent neuronal populations. Together, we conclude that PCG plays an important role in valence processing and serves as a critical hub to broadcast valence-specific signals globally to a distributed brain system.

## RESULTS

### PCG mediates sensory-induced aversion and reward-related behaviors

We examined the affective behavioral effect of various sensory cues and the involvement of PCG by infusing muscimol to silence PCG (Figures 1A and S1A). We first exploited a two-chamber place preference test<sup>38,41,42</sup> (see STAR Methods). Loud noise sound (80 dB sound pressure level [SPL]) or wind blow was applied whenever a naive mouse entered the predesignated “stimulation” chamber (Figures 1B and S1B). These aversive sensory stimuli greatly reduced the time spent by the animal in that chamber compared with control conditions without sensory stimulation (Figures 1B, 1C, S1B, and S1C), confirming the innately aversive nature of the auditory and somatosensory stimulation.<sup>38</sup> Moreover, the average speed of movements was much higher in the stimulation than non-stimulation chamber (Figure 1D), demonstrating that the animal rapidly escaped from the stimulation to the non-stimulation chamber. Silencing PCG activity significantly reduced this avoidance behavior and the locomotion increase induced by the aversive sensory stimuli, whereas saline infusion had no effects

(Figures 1C, 1D, S1C, and S1D). These results indicate that PCG plays a role in mediating sensory-induced aversion.

To examine whether PCG also plays a role in reward-related behavior, we adapted a sucrose preference test<sup>43,44</sup> (see STAR Methods). In this test, water-deprived mice could choose to lick from one of two bottles to acquire liquid of 2% sucrose or just water (Figure 1E). Muscimol inhibition of PCG activity resulted in a significant reduction of relative sucrose intake compared with the pre-injection condition, whereas saline had no effect (Figure 1F). This indicates that the activity of PCG also plays a role in mediating appetitive behavior.

Both aversive and rewarding stimuli can elicit arousal.<sup>11,45</sup> To study arousal induced by salient events, we measured the pupillary change in awake head-fixed animals responding to aversive (70 dB SPL noise and air puffs) and rewarding (sucrose water) stimuli (Figure 1G). Pupillary responses are known to reflect arousal state.<sup>46–48</sup> Both the aversive and appetitive sensory stimuli induced a large increase in pupil size in naive mice (Figures 1H and 1I), consistent with the notion that both positive and negative valence events can induce arousal.<sup>49–51</sup> Muscimol silencing of PCG activity significantly attenuated the arousal effect (Figures 1J and 1K), whereas saline had no effect (Figure S1E). Thus, PCG also plays a role in mediating arousal elicited by salient stimuli.

By applying fluorescence *in situ* hybridization with RNA probes (RNAscope) for vesicular glutamate transporter 2 (Vglut2) and vesicular GABA transporter (Vgat), we estimated the relative abundance and spatial distribution of glutamatergic and GABAergic neurons in PCG (Figure 1L). About 60% and 40% of neurons in PCG were found to be glutamatergic (i.e., Vglut2+) and GABAergic (Vgat+), respectively (Figure 1M). However, in its neighboring structure, DTN, GABAergic neurons predominated over glutamatergic neurons (Figure 1M).

### PCG glutamate and GABA neurons drive opposing valence-specific behaviors

As glutamatergic neurons were a slightly more dominant cell type in PCG, we tested the behavioral effect of optogenetic activation of these neurons by injecting adeno-associated virus (AAV) encoding Cre-dependent Channelrhodopsin-2 (ChR2) fused with enhanced yellow fluorescent protein (eYFP) (or eYFP alone as control) in Vglut2-Cre mice (Figures 2A and S2A). To assess the valence effect of the photoactivation, we employed an optogenetics-coupled real-time place preference (RTPP) test following previous studies.<sup>38,42</sup> In the test, whenever the mouse entered the designated stimulation chamber, light-emitting diode (LED) light pulses (470 nm, 5-ms duration, at 20 Hz) were continuously delivered through bilaterally implanted optic fibers above PCG until it exited. We found that ChR2-expressing mice spent significantly less time in the LED-On chamber than the eYFP control mice, with the latter spending about equal amounts of time in LED-On and LED-Off chambers (Figures 2B and 2C). Lower stimulation frequencies generated weaker effects (Figure S3A). The photoactivation also greatly suppressed food intake in hungry mice (food deprived for 24 h) (Figure S3B). These results suggest that PCG glutamatergic neurons drive negative-valence-specific behaviors. In addition, activation of these neurons acutely increased locomotion in an open field (Figures 2D and 2E).

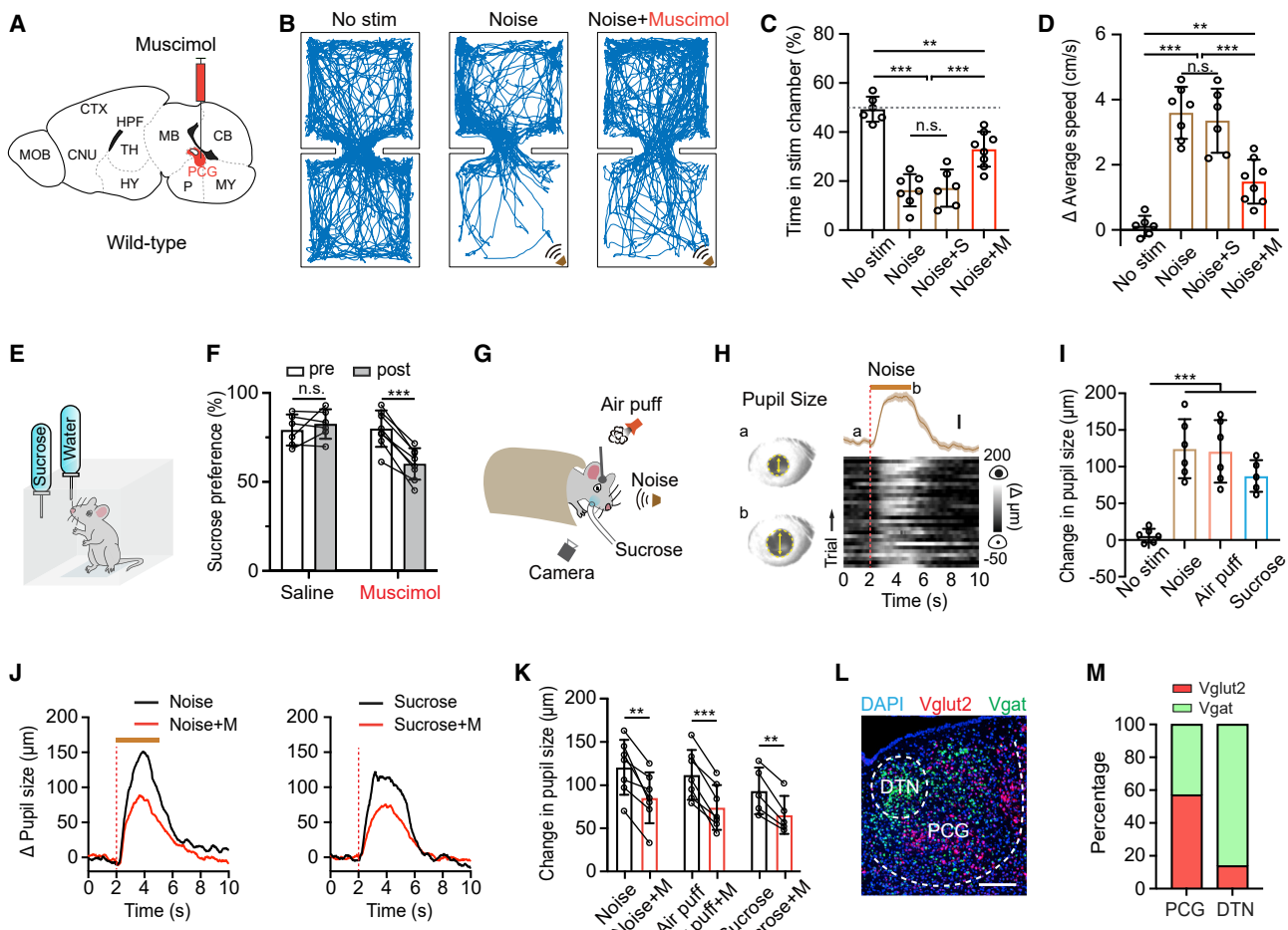


**Figure 1. PCG mediates sensory-induced aversion and reward-related behavior**

- (A) Schematic of a sagittal section of the mouse brain and infusion of fluorescent muscimol into PCG.
- (B) Example movement tracking traces in the place preference test for three mice in no-stimulation, noise alone (80 dB SPL), and noise plus PCG silencing (with muscimol) conditions.
- (C) Summary of percentage time spent in the stimulation chamber in different conditions. n = 6, 7, 6, 8 mice, respectively. The gray dash line marks 50% level. \*\*p < 0.01, \*\*\*p < 0.001, one-way ANOVA and post hoc test. "n.s.", not significant; S, saline; M, muscimol.
- (D) Summary of average locomotion speed in the stimulation chamber. n = 6, 7, 6, 8 mice, respectively. \*\*p < 0.01, \*\*\*p < 0.001, one-way ANOVA.
- (E) Schematic of sucrose preference test.
- (F) Summary of sucrose preference in the saline control and PCG silencing groups. n = 6 and 8 mice, respectively. Sucrose preference was quantified as the relative amount of sucrose water consumption during a 1 h test session (see STAR Methods). \*\*\*p < 0.001, paired t test.
- (G) Experimental configuration for measuring pupil size changes in responding to noise, air puffs, or sucrose water (5%) delivery in awake head-fixed condition.
- (H) Plot of pupil size changes in responding to noise (70 dB SPL, 3-s duration) for an example naive animal. Left: example images of pupil during baseline (a) and dilated (b) conditions. Yellow arrows mark the pupil diameter. Right: the plot of the average change in pupil size (mean ± SEM) aligned to the onset of noise stimulation (top) and Δ pupil size in each of 30 trials (bottom) for an example animal. The dotted red line indicates stimulus onset. The brown bar indicates the duration of noise.
- (I) Summary of peak pupil size changes in no-stimulation, noise, air puffs, and sucrose water delivery groups. n = 6, 6, 6, and 5 mice, respectively. \*\*\*p < 0.001, one-way ANOVA.
- (J) Plot of the average pupil size changes in responding to noise (left) or sucrose water (right) before (black) and after (red) silencing PCG with muscimol for an example mouse. The red dotted line indicates the onset time of stimulus. The brown bar indicates the duration of noise.
- (K) Summary of peak pupil size changes in responding to different sensory stimuli before and after silencing PCG with muscimol. n = 7, 7, and 5 mice, respectively. \*\*p < 0.01; \*\*\*p < 0.001, paired t test.
- (L) Representative RNAcope staining in PCG for the Vglut2 (red, Slc17a6) and Vgat (green, Slc32a1) probes. Blue represents DAPI staining. Scale bars, 200 μm.
- (M) Relative abundance of Vglut2+ (red) vs. Vgat+ (green) neurons. For each brain structure, n = 4 animals.

Error bar, SD in all plots.

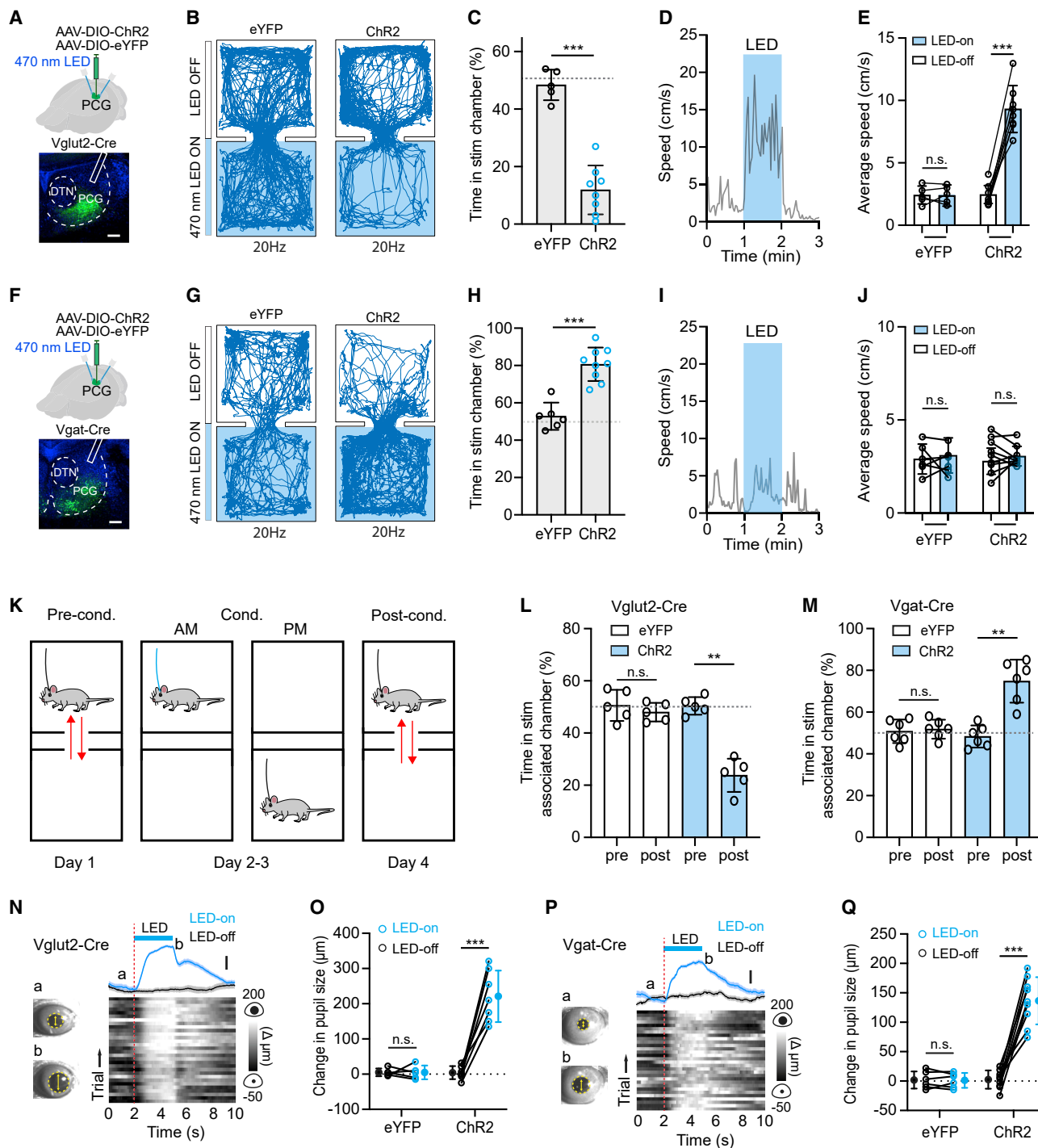


**Figure 2. PCG glutamate and GABA neurons drive avoidance and preference behavior, respectively**

(A) Top: experimental condition. Bottom: a representative confocal image showing the restricted expression of ChR2 within PCG. Scale bars, 200 μm.

(B) Example movement tracing for an animal in eYFP group or ChR2 group during a 20 min session of RTPP test with 20-Hz optical stimulation of PCG glutamatergic neurons.

(C) Percentage time spent in the LED-On chamber for the eYFP (n = 5 mice) and ChR2 (n = 8 mice) groups. The gray dash line marks 50% level. \*\*\*p < 0.001, t test.

(D) Plot of locomotion speed in an open field test for an example animal. The blue box marks the duration of LED stimulation of PCG Vglut2+ neurons.

(E) Average speed in LED-On (1 min) and LED-Off epochs. n = 5 and 8 mice for the eYFP and ChR2 group, respectively. \*\*\*p < 0.001, paired t test.

(F) Similar to (A) but for a Vgat-Cre mouse. Scale bars, 200 μm.

(G) Example movement tracing for a Vgat-Cre animal during a 20 min session of RTPP test with 20-Hz optical stimulation of PCG GABAergic neurons.

(legend continued on next page)

Next, we tested the effect of photostimulation of PCG GABAergic neurons by injecting the Cre-dependent ChR2 virus in Vgat-Cre mice (Figure 2F). Opposite to that of the glutamatergic neurons, the activation of the GABAergic neurons led to a strong preference for the LED-On chamber in the RTPP test (Figures 2G and 2H). This indicates a rewarding effect of these neurons, although no effect on locomotion was observed (Figures 2I and 2J). Thus, our data demonstrate that the activity of PCG glutamatergic and GABAergic populations drives negative and positive valence-specific behaviors, respectively.

Furthermore, we tested whether the acute valence effects of PCG neurons could support CPA or CPP.<sup>52,53</sup> To this end, we employed a 4-day test-conditioning-test strategy (Figure 2K) by selectively pairing optogenetic stimulation (20 Hz, 20 min) with one designated chamber over days 2–3. On day 4 (testing day), ChR2-expressing Vglut2-Cre animals exhibited avoidance from the paired LED-On chamber although no LED light was applied, while before conditioning (day 1) they did not show a preference for either chamber (Figure 2L). This result indicates that the photoactivation of the PCG glutamatergic neurons had enabled CPA. On the contrary, the photoactivation of PCG GABAergic neurons resulted in CPP (Figure 2M). Thus, our results further indicate that activities of PCG glutamatergic and GABAergic populations are associated with negative and positive valence, respectively.

Consistent with the affective effects, we found that activation of both PCG glutamatergic and GABAergic neurons led to enhanced arousal, as shown by the robust pupil dilation after the onset of light activation (20 Hz, duration 3-s), which was absent in the eYFP control mice (Figures 2N–2Q). Together, our results demonstrate opposing valence effects of activating PCG glutamatergic and GABAergic neurons, with both strongly enhancing arousal.

### PCG glutamate and GABA neurons respond to aversive and rewarding sensory events, respectively

Since PCG glutamatergic and GABAergic neurons drive negative and positive valence effects, respectively, we wondered whether they could be activated by aversive and rewarding sensory events, respectively. To test this, we performed optrode recording from photo-tagged neurons by injecting AAV-DIO-ChR2 into PCG of Vglut2-Cre/Vgat-Cre animals. The recording was performed in the awake head-fixed mouse, following our previous studies.<sup>10,38</sup> Of 298 units recorded in Vglut2-Cre mice, 121 neurons were identified as Vglut2+ neurons, as demonstrated by their time-locked

spike responses (latency < 3 ms) to applied blue light pulses (Figure 3A). As shown by an example ChR2-tagged glutamatergic neuron (Figure 3B) and the population response (Figure 3D), the majority of PCG Vglut2+ neurons (79/121) were excited by an aversive event (loud noise or air puffs) (Figures 3E and 3L). Most of them (60/79) were responsive to both the auditory and somatosensory stimuli (Figure 3E). For the remaining 177 untagged units, which presumably contained mainly GABAergic neurons, only 15.8% (28/177) responded to either noise or air puff stimulation, whereas the great majority were unresponsive (Figure 3E). Consistent with this data, in our recorded photo-tagged GABAergic neurons from Vgat-Cre mice (63 out of 112 units), only 9.5% (6/63) showed excitatory responses to the aversive auditory or somatosensory stimulation (Figures 3H, 3I, and 3L), whereas in the untagged population from Vgat-Cre mice, 69.3% (34/49) (presumably mainly glutamatergic neurons) did so (Figure 3I).

We then tested whether the GABAergic neurons could respond to rewarding sensory signals by delivering sucrose solution (5% w/v, 10 µL per trial) into the oral cavity of water-deprived mice via intraoral cheek fistulae (see STAR Methods). In photo-tagged GABAergic neurons (an example is shown in Figure 3C), the majority of them (72.2%, 39/54 units) showed increases in firing rate following the sucrose delivery (Figures 3J, 3K, and 3M), whereas 22.2% of the population (12/54) showed no change and 5.6% (3/54) showed a decrease in firing rate (Figure 3K). In the untagged population, only 6.2% (5/80) showed an excitatory response to sucrose, and the great majority showed no response (93.8%, 75/80) (Figure 3K). Consistent with this data, only 8.1% (3/37) of photo-tagged Vglut2+ neurons showed excitatory responses to sucrose, whereas in the untagged population, 68% (34/50) did so (Figures 3F and 3G). The glutamatergic and GABAergic neurons did not differ in spontaneous firing rate ( $3.1 \pm 1.8$  vs.  $3.4 \pm 1.6$  Hz, n = 121 and 63 neurons, p = 0.29, t test).

We also applied fiber photometry<sup>54,55</sup> recording of the ensemble Ca<sup>2+</sup> signal in PCG of freely moving mice (Figures 3N and 3Q) by injecting AAV-expressing Cre-dependent Ca<sup>2+</sup> indicator (AAV1-DIO-GCaMP6s) into Vglut2-Cre/Vgat-Cre mice.<sup>56</sup> Consistent with the single-unit data, the Vglut2+ population showed increases of Ca<sup>2+</sup> activity in response to noise, air puffs, and foot shocks (Figures 3O and 3P). By contrast, the activity of the Vglut2+ population was essentially not affected by sucrose delivery (Figures 3O and 3P). On the other hand, the Vgat+ population in water-deprived mice was preferentially activated by sucrose water, but not by noise, air puffs, or foot

(H) Percentage time spent in the LED-On chamber for the eYFP (n = 6 mice) and ChR2 (n = 9 mice) groups. \*\*\*p < 0.001, t test.

(I) Plot of locomotion speed in an open field test for an example Vgat-ChR2 animal.

(J) Average speed in LED-On (1 min) and LED-Off epochs. n = 6 and 9 mice, respectively. p > 0.05, paired t test.

(K) Timeline for CPA/CPP test.

(L and M) Percentage time spent in the LED-On chamber pre- and post-conditioning by activating PCG Vglut2+ neurons (L, n = 5 mice for each group) and Vgat+ neurons (M, n = 6 mice for each group). \*\*p < 0.01, paired t test.

(N) Plot of change in pupil size in responding to LED stimulation for an example Vglut2-Cre animal. Left: example images of pupil during baseline (a) and dilated (b) conditions. Right: plot of the average change in pupil size (mean ± SEM) aligned to the onset of optical stimulation (top) and Δ pupil size in each of 30 trials (bottom) for an example animal. Scale bars, 50 µm.

(O) Average change in pupil size in LED-On and LED-Off conditions. n = 5 and 7 mice, respectively. \*\*\*p < 0.001, paired t test.

(P) Plot of change in pupil size in responding to LED stimulation for an example Vgat-Cre animal. Scale bars, 50 µm.

(Q) Average change in pupil size in LED-On and LED-Off conditions. n = 6 and 9 mice, respectively. \*\*\*p < 0.001, paired t test.

Error bar, SD in all plots.

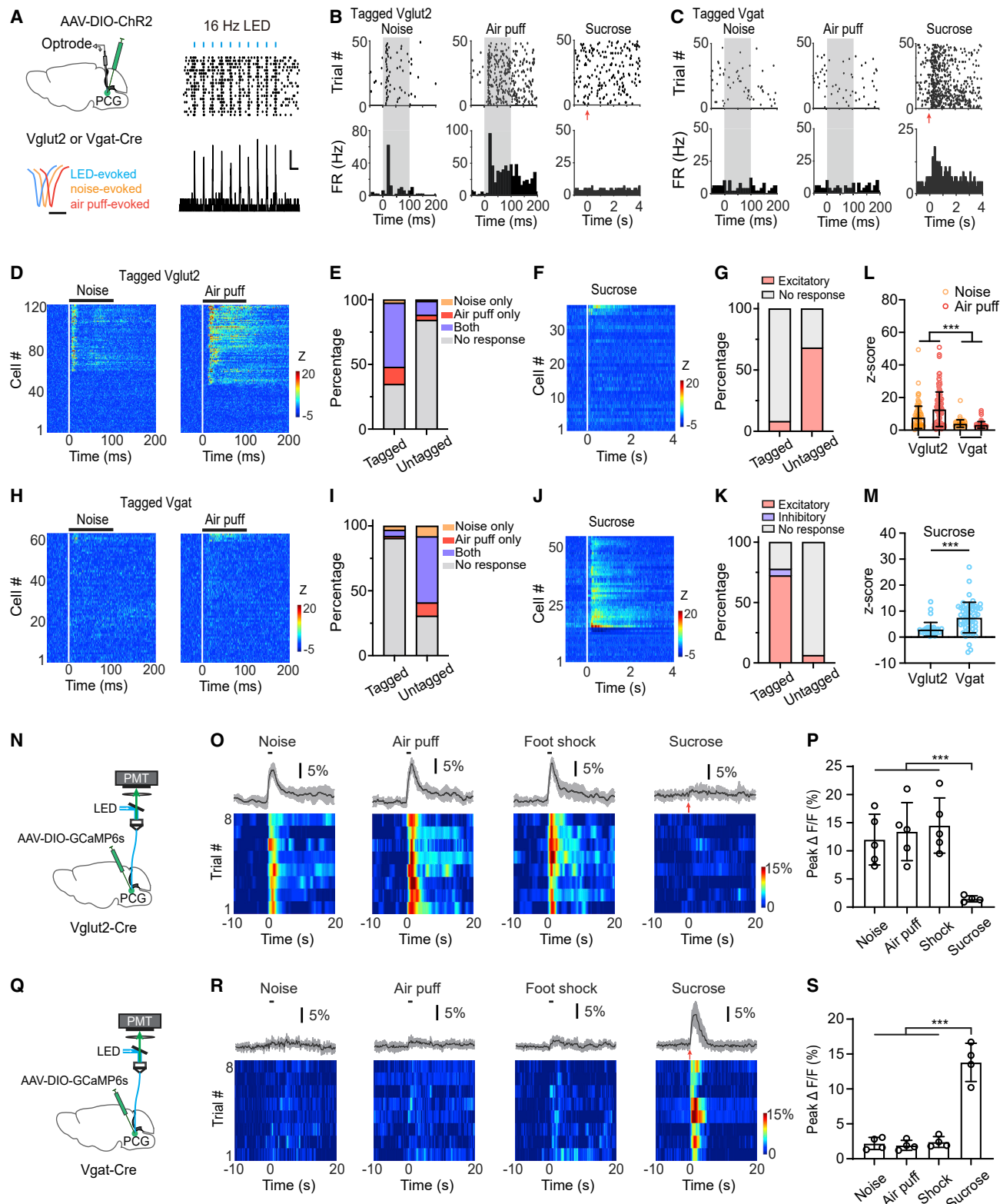


**Figure 3. PCG glutamate and GABA neurons are activated preferentially by aversive and reward sensory signals, respectively**

(A) Left: schematic of optrode recording from ChR2-tagged PCG glutamatergic or GABAergic neurons (top) and average waveforms of LED-evoked (blue), noise-evoked (orange), and air-puff-evoked (red) spikes from an example Vglut2+ unit (bottom). Scale bars, 0.5 ms. Right: raster plot (top) and peri-stimulus spike time histogram (PSTH, bottom) for LED-evoked spikes of an example tagged Vglut2+ neuron. Blue bars mark LED pulses (5-ms, 16 Hz). Scale bars, 5 Hz, 50 ms.

(legend continued on next page)  
Neuron 111, 1486–1503, May 3, 2023 1491

shocks (Figures 3R and 3S). Together, our results strongly suggest that PCG glutamatergic neurons are selectively activated by a range of aversive sensory stimuli across modalities, whereas its GABAergic population is preferentially activated by rewarding sensory signals.

### Suppression of PCG glutamate and GABA neurons attenuates sensory-induced aversion and appetitive behavior, respectively

Since PCG glutamatergic neurons drive negative valence effects and can be activated by aversive sensory stimuli, we wondered whether suppressing the activity of these neurons could specifically impair aversive sensory-induced behaviors. We inhibited these neurons by injecting AAV-expressing Cre-dependent ArchT in Vglut2-Cre mice and applying green LED light (Figure 4A). The photo-inhibition of the Vglut2+ neurons alone did not induce any place preference/avoidance or any change in pupil size (Figures S4A–S4E), suggesting that the baseline activity of these neurons might not significantly affect the affective state. However, the optogenetic inhibition greatly reduced the avoidance behavior (Figures 4B and 4C), locomotion increase (Figure 4D), and pupil dilation (Figures 4E, 4F, S5A, and S5B) induced by aversive sensory stimulation, without generating a significant effect on reward-related behavior (Figures S5C and S5D). Thus, our data suggest that the sensory-evoked activity of PCG glutamatergic neurons is specifically required for aversive sensory-induced behavior.

We further tested the involvement of PCG GABAergic neurons in reward-related behavior, by injecting AAV-expressing Cre-dependent ArchT in Vgat-Cre mice (Figure 4G). The optogenetic inhibition of the Vgat+ neurons alone did not produce any valence effect or changes in pupil size (Figures S4F–S4J). In

the sucrose preference test, we compared LED-On vs. LED-Off epochs. The photo-inhibition resulted in a significant reduction of sucrose intake in the ArchT-expressing group, whereas no effect was observed in GFP control mice (Figure 4H). It also greatly reduced pupil dilation induced by rewarding sucrose stimulation (Figures 4I and 4J). On the other hand, the optogenetic inhibition of the Vgat+ neurons had no effect on the avoidance behavior (Figures S5E and S5F), locomotion increase (Figure S5G), or pupil dilation (Figures S5H and S5I) induced by aversive sensory stimulation. These data suggest that the sensory-evoked activity of PCG GABAergic neurons is specifically required for sensory-induced appetitive behavior.

### PCG glutamate and GABA neurons share similar projection patterns

Since the activation of PCG glutamatergic and GABAergic neurons produced very different behavioral outcomes, we wondered whether they projected to different downstream targets. To address this question, we injected AAV-FLEX-GFP into the PCG of Vglut2-Cre or Vgat-Cre mice (Figures 5A and 5C). To our surprise, GFP-labeled glutamatergic and GABAergic PCG axons exhibited similar projection patterns (Figures 5B and 5D), mainly on the ipsilateral side (Figures 5E and 5F). Among the diverse brain regions targeted by PCG, structures such as the mediodorsal nucleus of the thalamus (MD), paraventricular thalamus (PVT), lateral hypothalamic areas (LHAs), ventral tegmental area (VTA), lateral preoptic area (LPO), and medial septum-diagonal band nucleus (MS/DB) were strongly innervated by both the glutamatergic and GABAergic axons (Figures 5E and 5F). Most of these structures have been implicated in motivated behaviors.<sup>6,7,10,38,52,57,58</sup> Therefore, PCG glutamatergic and GABAergic neurons both feed valenced sensory

(B and C) Raster plot (top) and PSTH (bottom) for spike responses of an example PCG Vglut2+ neuron (B) or Vgat+ neuron (C) to 70 dB SPL noise (left), air puff (middle), and sucrose water delivery (right). The gray box marks the duration of sensory stimulation. Red arrow indicates the onset of sucrose water delivery.

(D) Heatmap plot of time-dependent Z score for spike responses of all tagged PCG Vglut2+ neurons ( $n = 121$  cells from 5 mice) to noise (left) or air puff (right). Each row represents a single neuron. The black bar above indicates the duration of the stimulation (onset is at time zero).

(E) Proportions of neurons activated by noise only, by air puff only, by both, or by none in ChR2-tagged ( $n = 121$ ) and untagged ( $n = 177$  from 5 mice) groups of Vglut2-Cre mice.

(F) Heatmap plot of time-dependent Z score for spike responses of all tagged PCG Vglut2+ neurons ( $n = 37$  from 3 mice) to sucrose water stimulation.

(G) Proportion of neurons activated by sucrose water delivery for tagged ( $n = 37$ ) and untagged populations ( $n = 50$ ).

(H) Heatmap plot of time-dependent Z score for spike responses of all recorded tagged Vgat+ units ( $n = 63$  from 4 mice) to 70 dB SPL white noise (left) or air puff (right).

(I) Proportions of neurons activated by noise only, by air puff only, by both, or by none in ChR2-tagged ( $n = 63$ ) and untagged ( $n = 49$  from 4 mice) groups of Vgat-Cre mice.

(J) Heatmap plot of Z score for spikes of all recorded tagged Vgat+ units in response to sucrose consumption ( $n = 54$  from 4 mice).

(K) Proportions of neurons showing excitatory (light red), inhibitory (blue), or no (gray) responses to sucrose water in ChR2-tagged ( $n = 54$ ) and untagged ( $n = 80$ ) populations in Vgat-Cre mice.

(L) Comparison of the peak Z score within a 100 ms window in responding to noise or air puff for tagged Vglut2+ ( $n = 121$ ) and Vgat+ ( $n = 63$ ) neurons. \*\*\* $p < 0.001$ , one-way ANOVA.

(M) Comparison of the peak Z score within a 0–2 s window in responding to sucrose water delivery for Vglut2+ ( $n = 37$ ) and Vgat+ ( $n = 54$ ) neurons. \*\*\* $p < 0.001$ , t test.

(N) Schematic of fiber photometry imaging from PCG Vglut2+ neurons.

(O) Top: average percentage fluorescence change ( $\pm$  SD) in responding to noise, air puffs, foot shocks, or sucrose water for an example Vglut2-Cre mouse. Bottom: heatmap plot of fluorescence changes in all trials. The black bar indicates stimulus duration (1 s).

(P) Summary of peak fluorescence changes in responding to different stimuli in Vglut2-Cre mice. \*\*\* $p < 0.001$ , one-way ANOVA,  $n = 5, 5, 5$ , and 4 mice from left to right.

(Q) Schematic of fiber photometry imaging from PCG Vgat+ neurons.

(R) Similar to (O) but for a Vgat-Cre mouse.

(S) Summary of fluorescence changes for Vgat-Cre mice. \*\*\* $p < 0.001$ , one-way ANOVA,  $n = 4, 4, 4$ , and 4 mice.

Error bar, SD in all plots.

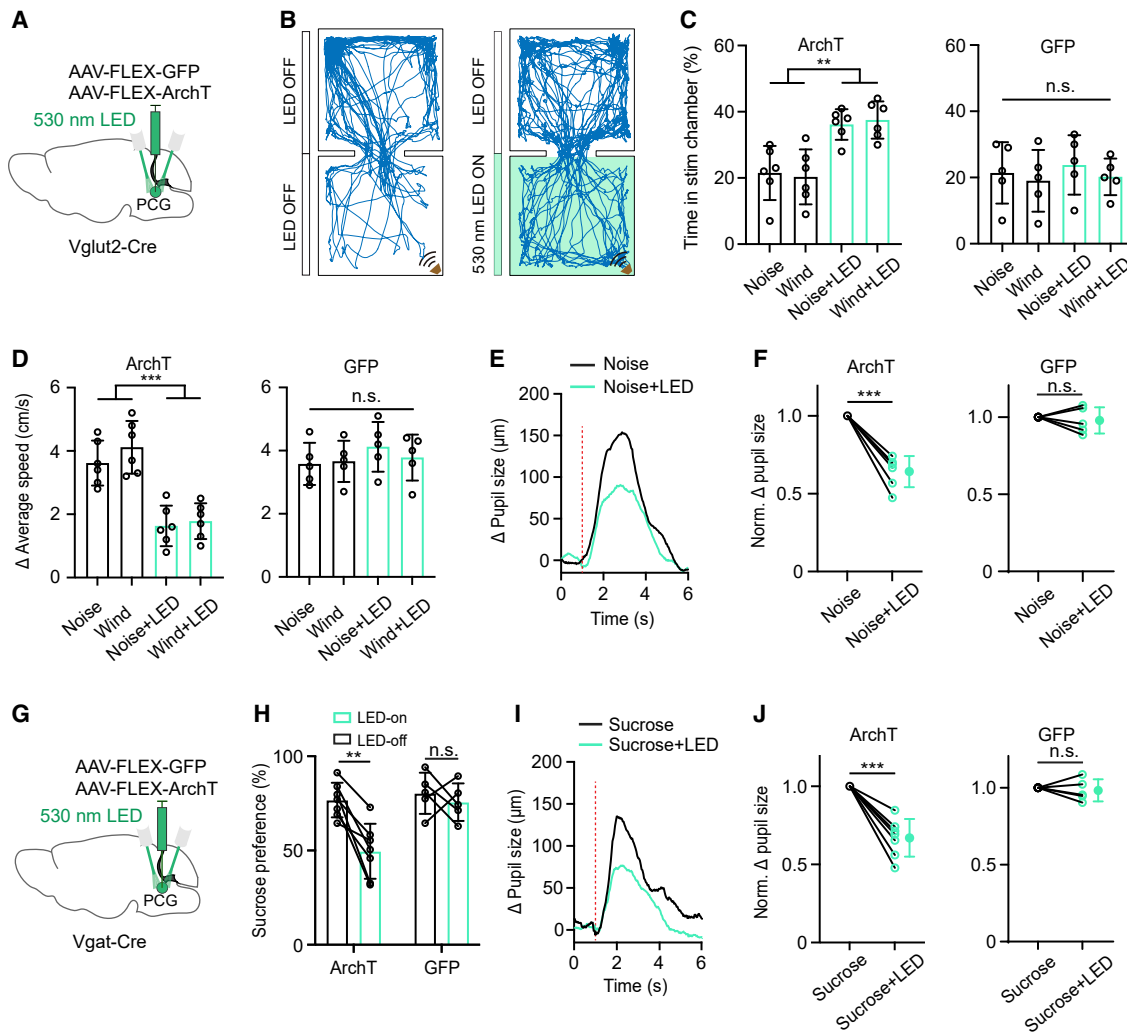


**Figure 4. Effects of silencing PCG glutamate and GABA neurons on sensory-induced behaviors**

(A) Schematic viral injection for silencing PCG Vglut<sup>2+</sup> neurons.

(B) Example movement tracking in RTTP test in noise stimulation (left) and noise plus green LED (right) condition.

(C) Summary of percentage time spent in the stimulation chamber in the ArchT (left, n = 6 mice for each subgroup) and GFP groups (right, n = 5 mice for each subgroup) under different conditions. \*\*p < 0.01, one-way ANOVA.

(D) Summary of average speed increased in the stimulation chamber in the ArchT (left, n = 6 mice for each subgroup) and GFP groups (right, n = 5 mice for each subgroup) under different conditions. \*\*\*p < 0.001, one-way ANOVA.

(E) Average change in pupil size in responding to noise alone (black) and noise plus LED (green) for an example Vglut2-Cre mouse. The red dotted line indicates the stimulus onset.

(F) Comparison of normalized Δ pupil size between noise alone and noise plus LED conditions in ArchT (n = 6 mice) and GFP (n = 5 mice) groups. \*\*\*p < 0.001, paired t test.

(G) Schematic viral injection for silencing PCG Vgat<sup>+</sup> neurons.

(H) Summary of sucrose preference without and with LED illumination in the Arch T (n = 7 mice) and GFP (n = 5 mice) groups. \*\*p < 0.01, paired t test.

(I) Average pupil size changes in responding to sucrose alone (black line) and sucrose plus LED (green line) for an example mouse. The red dotted line indicates stimulus onset.

(J) Comparison of normalized Δ pupil size between sucrose alone and sucrose plus LED conditions in the ArchT (n = 7 mice) and GFP (n = 5 mice) groups. \*\*\*p < 0.001, paired t test.

Error bar, SD in all plots.

information into a large network that is highly engaged in processing emotionally salient information.

We further explored intra-PCG connectivity by specifically expressing ChR2 in PCG GABAergic neurons in Vgat-Cre::Ai14

mice. In slice preparations, we performed whole-cell recording selectively from PCG glutamatergic neurons (tdTomato<sup>-</sup>) in the presence of tetrodotoxin (TTX) and 4-aminopyridine (4AP) while optically stimulating PCG GABAergic neurons (Figure S6).

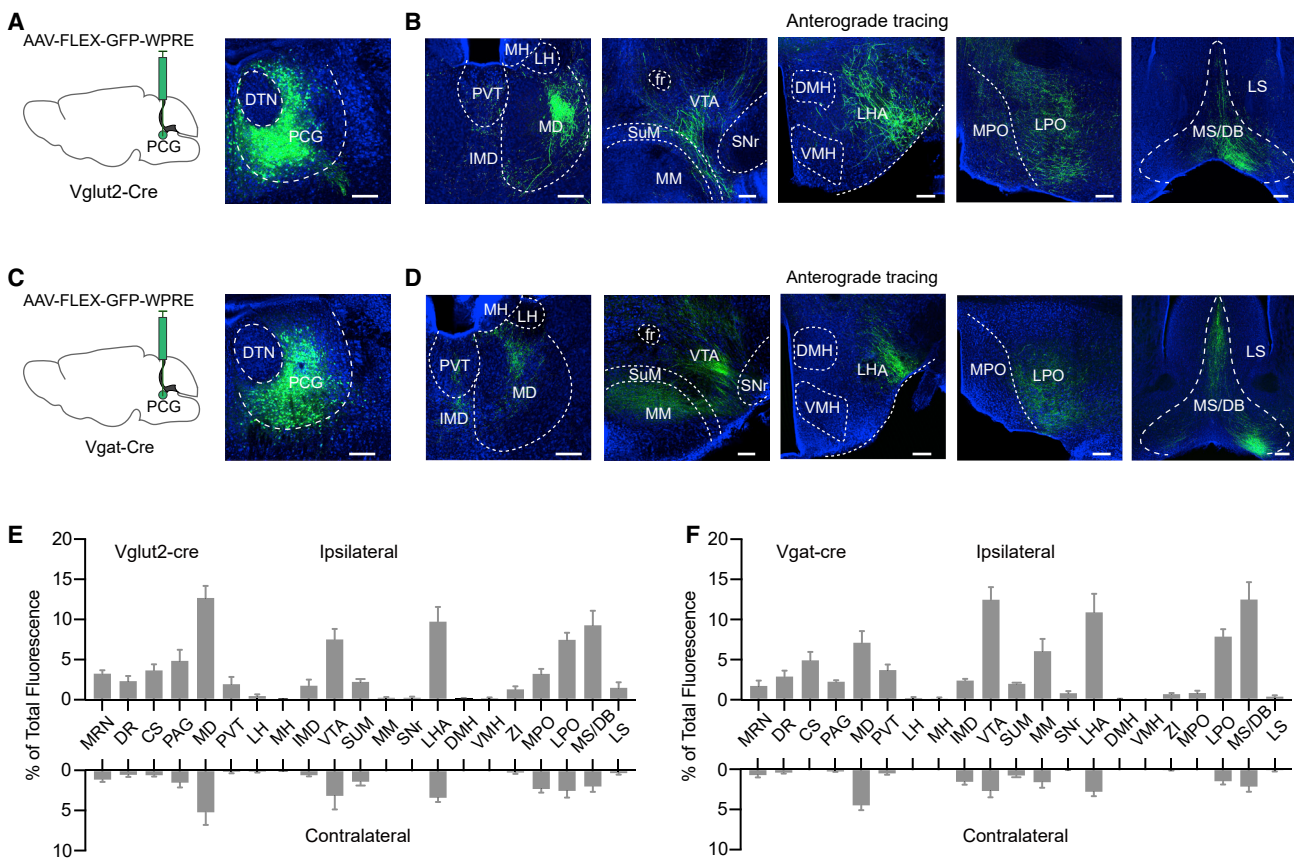


**Figure 5. Projection targets of PCG glutamatergic and GABAergic neurons**

(A and B) Schematic viral injection (A, left) and fluorescence expression at the injection site (A, right) and GFP-labeled axons in major target regions (B) in a Vglut2-Cre mouse. Blue represents Nissl staining. Scale bars, 200  $\mu$ m.

(C and D) Target regions of PCG Vgat+ axons in a Vgat-Cre mouse. Scale bars, 200  $\mu$ m.

(E and F) Quantification of relative fluorescence density of GFP-labeled axons in different downstream regions of PCG Vglut2+ (E, n = 3 animals) and Vgat+ (F, n = 3 animals) neurons in the ipsilateral and contralateral side. Error bar, SD in all plots.

Abbreviations: see STAR Methods.

Light-evoked monosynaptic inhibitory postsynaptic currents (IPSCs) were observed in the glutamatergic neurons, indicating that the GABAergic neurons can suppress local glutamatergic neurons. This local inhibition suggests a competitive interaction between the pathways mediated by the two PCG cell types, which may contribute to their opposing valence effects.

### PCG mediates aversion and reward behaviors through distinct downstream targets

To further examine which of the downstream projections mediates the PCG-dependent behavioral effects, we optically activated ChR2-expressing axonal terminals from PCG glutamatergic (Figure 6A) or GABAergic neurons (Figure 6G) in each of the aforementioned target areas and at the same time silenced PCG cell bodies with muscimol to prevent the potential spread of antidromic spikes to undesired targets. Bilateral stimulation of PCG glutamatergic axons in the MD, VTA, LHA, and MS/DB resulted in avoidance behavior (Figures 6B and 6C) and enhanced arousal (Figures 6E and 6F). In addition, the stimula-

tion of PCG-to-MD, PCG-to-LHA, and PCG-to-MS/DB axons significantly increased locomotion speed (Figure 6D). However, the stimulation of the PCG projections to PVT and LPO, in general, had no obvious effect on aversion (Figure 6C), arousal (Figure 6F), or locomotion speed (Figure 6D), except that stimulation of the PCG-to-LPO projection produced weak aversion (Figure 6C). Different from the glutamatergic projections, stimulation of the PCG GABAergic projections VTA, LHA, and MS/DB (but not MD) resulted in place preference (Figures 6H and 6I) and enhanced arousal (Figures 6K and 6L). The stimulation of the GABAergic projections to LPO, PVT, and MD did not produce significant behavioral effects (Figures 6I, 6J, and 6L), and none of the GABAergic projections tested had an effect on locomotion (Figure 6J). Together, these data suggest that PCG glutamatergic and GABAergic neurons may mediate aversion and reward-related behaviors through overlapping yet distinguishable downstream targets.

We further tested the involvement of specific PCG projections in sensory-induced aversion or reward-related behavior by

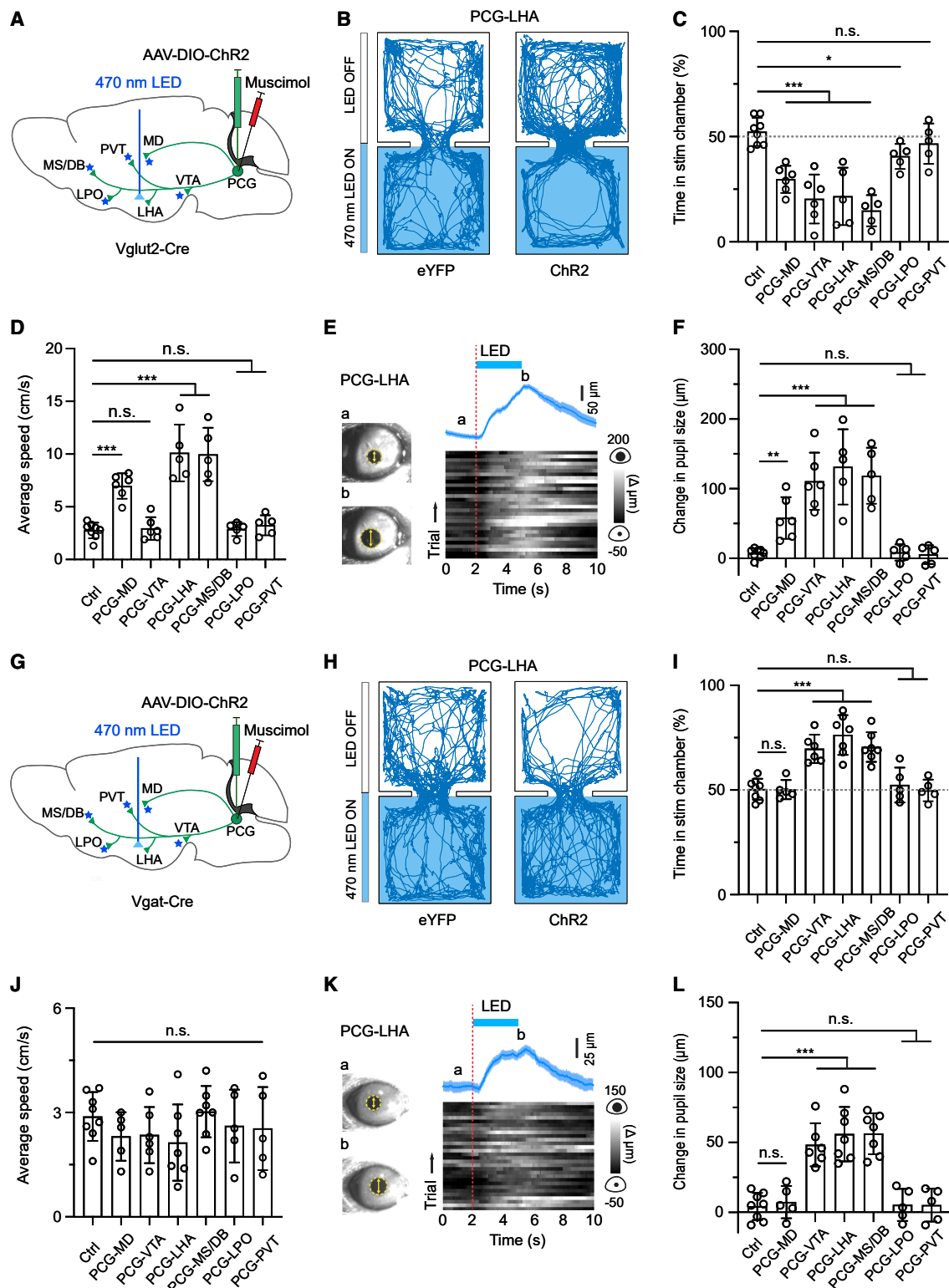


**Figure 6. PCG glutamatergic and GABAergic neurons mediate behavioral effects through distinguishable downstream projections**

(A) Schematic viral injection and optical stimulation of PCG axon terminals in different target regions separately in Vglut2-Cre mice while silencing PCG cell bodies with muscimol.

(B) Movement tracking traces for an example eYFP and ChR2 animal in RTPP test with optical stimulation applied to PCG glutamatergic projections in LHA.

(legend continued on next page)

optogenetically inhibiting PCG glutamatergic/GABAergic axons in two selected targets, VTA and LHA (Figures 7A, 7E, and 7I), after injecting AAV encoding Cre-dependent halorhodopsin (eNpHR3.0). Inhibiting the glutamatergic axon terminals in both VTA and LHA significantly attenuated the avoidance behavior (Figures 7B and 7F) and pupil dilation (Figures 7D, 7H, S7A, S7B, S7D, and S7E) induced by aversive, but not rewarding, sensory stimulation (Figures S7C and S7F). In addition, inhibiting the glutamatergic axon terminals in LHA (Figure 7G), but not VTA (Figure 7C), reduced the locomotion effect. On the other hand, inhibiting the GABAergic projections to both VTA and LHA resulted in a reduction of sucrose intake (Figures 7J and 7L). It also attenuated the pupil dilation induced by rewarding sucrose stimulation (Figures 7K and 7M) but not that induced by aversive sensory stimulation (Figures S7G–S7L). These results confirm that PCG relays valence-specific signals to multiple targets to mediate sensory-induced aversion and reward-related behaviors.

### Overlapping but distinguishable inputs to PCG glutamate and GABA neurons

Finally, we sought to identify monosynaptic inputs to PCG glutamatergic and GABAergic neurons by applying cell-type-specific retrograde tracing with pseudotyped glycoprotein-deficient rabies virus<sup>59–61</sup> (Figures 8A and 8E). We found that although the glutamatergic and GABAergic neurons shared some common input sources, the strongest input sources were clearly different between these two populations. The excitatory neurons received the strongest input from the PRN (Figures 8C and 8D), while the inhibitory neurons from the OFC (Figures 8G and 8H), which has been shown to be involved in regulating emotional and reward-related behaviors.<sup>62–65</sup> Thus, PCG glutamatergic and GABAergic neurons receive distinguishable inputs, possibly conferred by their differential roles in valence processing.

## DISCUSSION

In this study, with cell-type specific approaches, our data have elucidated a circuit mediated by PCG (Figure S8C) to relay valence-specific sensory information into an extended valence processing network. Our results showed that PCG glutamatergic

and GABAergic neurons play opposing functional roles: the glutamatergic neurons are activated by aversive sensory stimuli and drive avoidance behavior, whereas the GABAergic neurons are activated by rewarding stimuli and drive appetitive behavior. In addition, the activity of these two cell populations is sufficient for the formation of an association of initially neutral sensory cues with reward/aversion. Our results suggest that PCG may serve as a critical node in bottom-up sensory pathways to process valence-specific information of incoming sensory signals and mediate appropriate behavioral responses.

### PCG encodes opposite valences via two distinct neuronal populations

Our previous studies have suggested that PCG can provide sensory input to the MS<sup>37</sup> and that the glutamatergic projection from the MS to the lateral habenula can account at least partially for the avoidance behavior induced by aversive sound stimuli.<sup>38</sup> However, whether PCG itself is also involved in valence processing is unclear and functional roles of PCG beyond a simple sensory relay remain poorly understood. In this study, we demonstrated that in PCG, a sensory information processing stage preceding the classic limbic system, valence processing already occurs. Conforming to the definition of valence coding neurons,<sup>3,11,27,55</sup> PCG neurons have differential responses to aversive and reward sensory stimuli: the glutamatergic neurons are selectively activated by aversive cues across multiple sensory modalities while the GABAergic neurons are preferentially activated by reward cues. The behavioral outcomes of the activation of these neuronal populations are also negative and positive valence specific, avoidance, and preference, respectively. Consistent with the notion that both reward and punishment can induce emotional arousal,<sup>11,66</sup> the activation of both cell types leads to elevated arousal levels. In addition, the ability to induce CPA or CPP by activating PCG neurons alone further supports that PCG activity is not simply for the sensory relay but contains valence-specific information. Thus, our results have revealed a previously unrecognized functional role of PCG in valence processing. Through two separate neuronal populations, PCG can encode both negative and positive valences and mediate valence-specific motivational behaviors. Interestingly, the co-existence of negative valence representing

(C) Percentage time spent in the LED-On chamber with stimulation of PCG glutamatergic projections to different target regions. \*p < 0.05, \*\*p < 0.001, one-way ANOVA and post hoc test; n = 8, 6, 6, 5, 5, 5, and 5 mice from left to right. Control mice were pooled.

(D) Average locomotion speed during stimulation of PCG glutamatergic projections to different targets in the open-field test. \*\*\*p < 0.001, one-way ANOVA; n = 8, 6, 6, 5, 5, and 5 mice from left to right.

(E) Pupil size changes in responding to activation of PCG-to-LHA glutamatergic axons (30 trials) in an example animal. The trace on top represents as mean ± SEM.

(F) Summary of peak pupil size changes elicited by stimulating PCG glutamatergic projections to different targets. \*\*p < 0.01, \*\*\*p < 0.001, one-way ANOVA; n = 8, 6, 6, 5, 5, and 5 mice from left to right.

(G) Similar to (A) but in Vgat-Cre mice.

(H) Movement tracking traces for an example animal in the RTPP test with optical stimulation applied to PCG GABAergic projections in LHA.

(I) Percentage time spent in the LED-On chamber with stimulation of PCG GABAergic projections to different target regions. \*\*\*p < 0.001, one-way ANOVA; n = 8, 5, 6, 7, 7, 5, and 5 mice from left to right.

(J) Average locomotion speed during stimulation of PCG GABAergic projections to different target regions in the open field test. p > 0.05, one-way ANOVA; n = 8, 5, 6, 7, 7, 5, and 5 mice from left to right.

(K) Pupil size changes in responding to activation of PCG-to-LHA GABAergic axons in an example animal.

(L) Summary of peak pupil size changes elicited by stimulating PCG GABAergic projections to different target regions. \*\*\*p < 0.001, one-way ANOVA; n = 8, 5, 6, 7, 7, 5, and 5 mice from left to right. Control mice were pooled.

Error bar, SD in all plots.

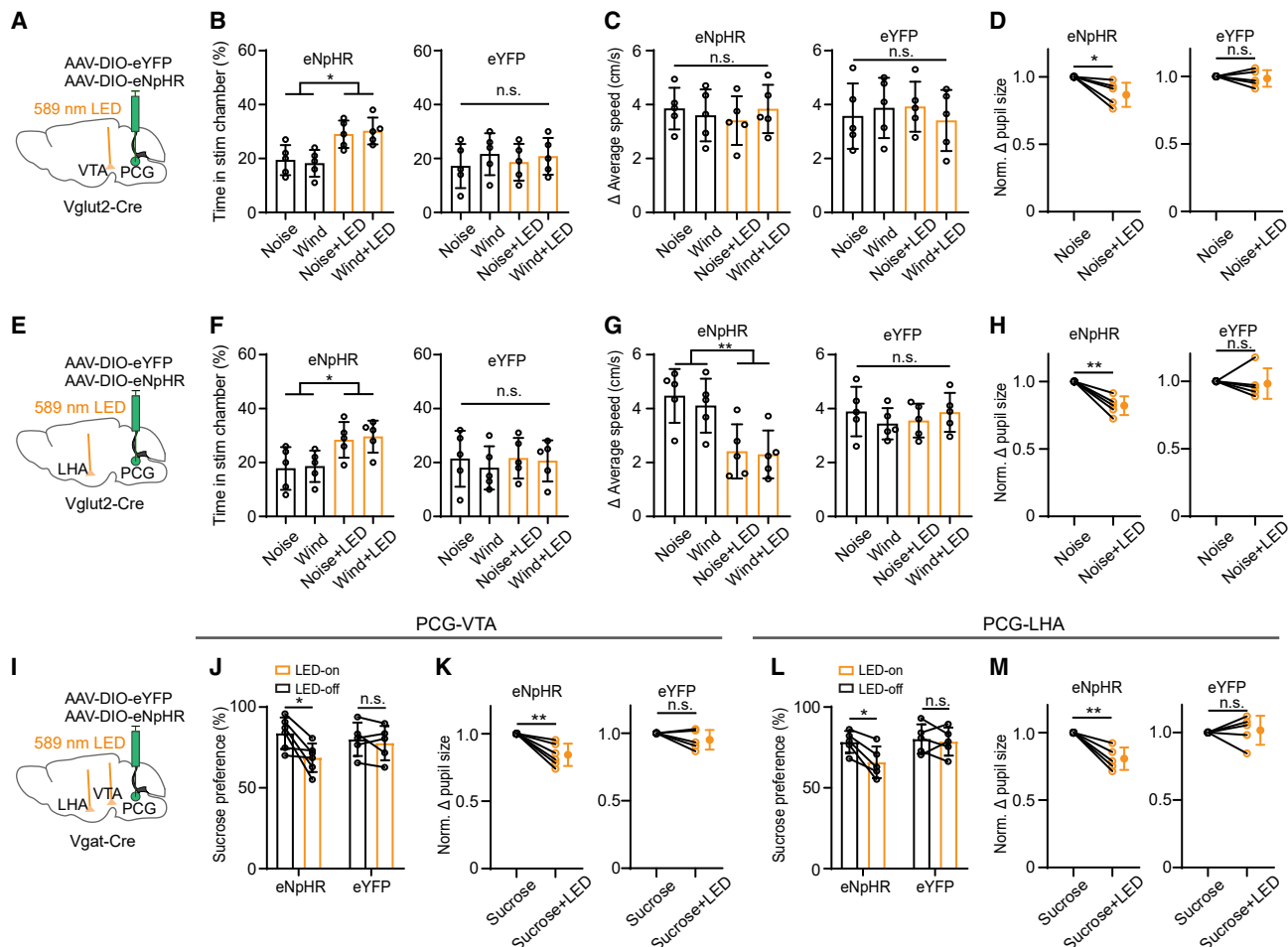


**Figure 7. Silencing PCG glutamatergic and GABAergic projections to specific targets attenuates aversion and reward-related behavior, respectively**

(A) Optogenetic silencing (bilaterally) of PCG glutamatergic axon terminals in VTA.

(B) Summary of percentage time spent in the stimulation chamber in eNpHR ( $n = 5$  mice for each subgroup) and eYFP ( $n = 5$  mice for each subgroup) groups under different conditions. \* $p < 0.05$ , one-way ANOVA and post hoc test.

(C) Summary of increases in average speed in the stimulation chamber.  $p > 0.05$ , one-way ANOVA.

(D) Normalized  $\Delta$  pupil size in noise alone and noise plus LED conditions in eNpHR ( $n = 5$  mice) and eYFP ( $n = 5$  mice) groups. \* $p < 0.05$ , paired t test.

(E) Optogenetic silencing (bilaterally) of PCG glutamatergic axon terminals in LHA.

(F) Summary of percentage time spent in the stimulation chamber in the eNpHR ( $n = 5$  mice for each subgroup) and eYFP ( $n = 5$  mice for each subgroup) groups. \* $p < 0.05$ , one-way ANOVA.

(G) Summary of increases in average speed in the stimulation chamber in eNpHR ( $n = 5$  mice for each subgroup) and eYFP ( $n = 5$  mice for each subgroup) groups. \*\* $p < 0.01$ , one-way ANOVA.

(H) Normalized  $\Delta$  pupil size in noise alone and noise plus LED conditions in eNpHR ( $n = 5$  mice) and eYFP ( $n = 5$  mice) groups. \*\* $p < 0.01$ , paired t test.

(I) Optogenetic silencing of PCG GABAergic axon terminals in the LHA and VTA separately.

(J) Summary of sucrose preference without and with LED illumination in eNpHR ( $n = 6$  mice) and eYFP ( $n = 5$  mice) groups. \* $p < 0.05$ , paired t test.

(K) Normalized  $\Delta$  pupil size in sucrose alone and sucrose plus LED conditions in eNpHR ( $n = 6$  mice) and eYFP ( $n = 5$  mice) groups. \*\* $p < 0.01$ , paired t test.

(L) Summary of sucrose preference without and with LED illumination in eNpHR ( $n = 5$  mice) and eYFP ( $n = 5$  mice) groups. \* $p < 0.05$ , paired t test.

(M) Normalized  $\Delta$  pupil size in sucrose alone and sucrose plus LED conditions in eNpHR ( $n = 5$  mice) and eYFP ( $n = 5$  mice) groups. \*\* $p < 0.01$ , paired t test.

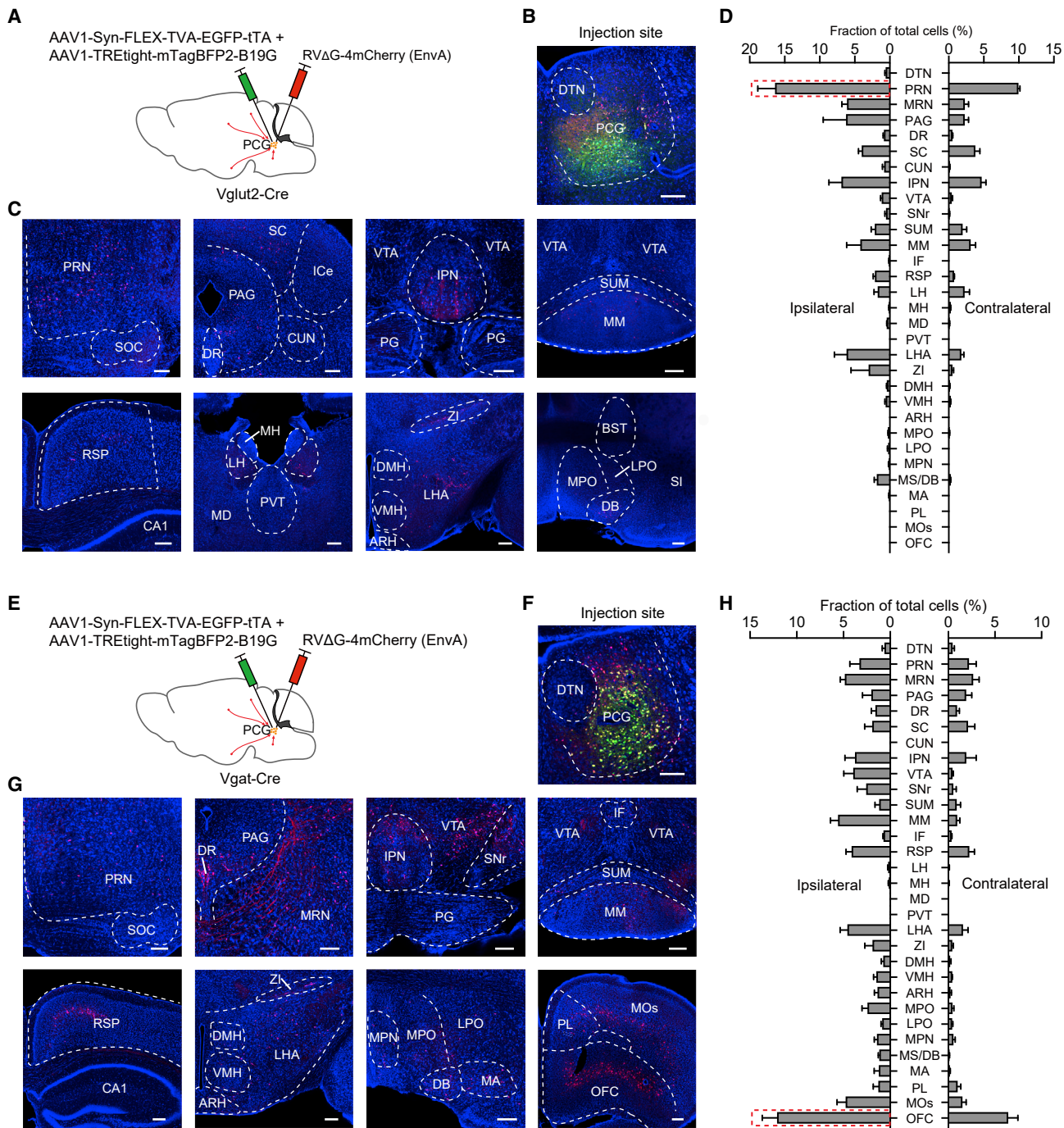
Error bar, SD in all plots.

glutamatergic neurons and positive valence representing GABAergic neurons in the same structure is also found for several other brain areas including the ventral pallidum,<sup>67,68</sup> MS,<sup>10,38</sup> bed nucleus of the stria terminalis (BST),<sup>69</sup> LHA,<sup>6,7</sup> and medial preoptic area (MPO).<sup>55</sup> This suggests that coding of opposite valences by neuronal populations defined by inher-

ently opponent neurotransmitter types may be a general strategy employed in the mammalian nervous system.

#### Broad integration of information by PCG

The anatomical connections of different cell types in PCG, to our knowledge, have not been characterized previously.<sup>70</sup>

**Figure 8. Monosynaptic inputs to PCG glutamatergic and GABAergic neurons**

(A) Strategy for cell-type-specific retrograde tracing of monosynaptic inputs to PCG glutamatergic neurons using pseudotyped rabies virus in Vglut2-Cre mice.

(B and C) Example images of fluorescence expression at the injection site (B) and in different input regions (C). Scale bars, 200  $\mu$ m.

(D) Quantification of the relative number of cells innervating PCG Vglut2+ neurons in different brain regions in the ipsilateral (left) and contralateral (right) side ( $n = 3$  animals; bar = SD).

(E–H) Similar to (A)–(D) except for tracing of monosynaptic inputs to PCG Vgat+ neurons ( $n = 3$  animals). Scale bars, 200  $\mu$ m.

Abbreviations: see STAR Methods.

The cell-type-specific monosynaptic retrograde tracing results indicate that the PCG glutamatergic and GABAergic neurons receive inputs from broad, partially overlapping sources (Figure 8), including midbrain, thalamic, hypothalamic, basal forebrain, and cortical regions. The profiles of strengths of their diverse inputs are clearly different. The most prominent input to the glutamatergic neurons arises from the PRN, which is a multisensory nucleus.<sup>71</sup> The PRN is thought as a sensorimotor interface<sup>72</sup> and multisensory information can be relayed via PRN to other brain structures. Thus, it is likely that PCG glutamatergic neurons receive bottom-up multisensory input from the PRN, which sits at a lower level in the hierarchy based on the onset latency of responses to aversive sound stimuli.<sup>37</sup>

Although PCG GABAergic neurons also receive bottom-up input from the PRN, their most prominent input is interestingly from the OFC (Figure 8), which has been shown to be involved in processing reward value, mood, and emotion.<sup>64,73</sup> Such circuit design may conform to the nature of reward cues. Although there are many innately aversive sensory stimuli, innately rewarding cues are few and often the assignment of positive valence strongly depends on the context, prior experience, or internal states of the animal.<sup>12,74</sup> Likely, the assignment of positive valence has to be strongly modulated by top-down input, e.g., orbital frontal cortical input that represents appraisals of surroundings or information about prior knowledge. In addition, OFC has been shown to encode high-level cognitive signals.<sup>65,75</sup> By exerting influence on the valence-specific expression of motivational behavior via its projection to PCG, OFC can then play a role in the cognitive regulation of emotion. Considering the prominent top-down inputs from the frontal cortex to its GABAergic neurons, PCG may not simply serve as an important node in bottom-up sensory pathways but can also play other roles in emotional behaviors.

It is worth noting that PCG also receives input from the interpeduncular nucleus (IPN), which is involved in addiction, anxiety, and mood regulation.<sup>76,77</sup> In addition, it receives moderate excitatory input from the lateral habenula, a structure involved in the processing of aversive information and mood,<sup>78</sup> as well as from other regions known to be involved in valence processing such as VTA and LHA.<sup>7,14,79</sup> Taken together, the broad inputs (including both bottom-up and top-down) to both the PCG glutamatergic and GABAergic neurons suggest that their valence coding properties may be modulated by a multitude of factors and their activity may be modulated at different timescales depending upon the source of input.

### PCG broadcasts valence-specific information to an extended brain network

Our anterograde tracing results indicate that axons from the PCG may be divided into two ascending streams (dorsal and ventral streams, see Figure S8C) that innervate various targets in the midbrain, thalamus, hypothalamus, and basal forebrain. Outputs of its glutamatergic and GABAergic neurons are directed to essentially the same targets, including MD, LHA, VTA, MS/DB, LPO, MPO, medial mammillary nucleus (MM), midbrain reticular nucleus (MRN), superior central nucleus raphe (CS), and periaqueductal gray (PAG). PCG neurons, especially

the glutamatergic population, send dense projections to MD, which is known to form reciprocal interactions with the prefrontal cortex and play a critical role in complex cognitive behaviors and decision making.<sup>80,81</sup> PCG also innervates MS/DB, supramammillary nucleus (SuM), and MM, which are involved in regulating hippocampal related functions including memory processing, spatial learning, navigation, and theta oscillations.<sup>82–84</sup> We also found obvious projections in the MRN and CS. The former is involved in locomotion<sup>85</sup> and the latter plays a pivotal role in regulating mood, fear, and anxiety<sup>86,87</sup> as well as memory consolidation.<sup>88</sup> Therefore, it is likely that PCG activity can engage a large extended brain network and that it serves as an important hub to control a set of functions even beyond valence processing.

Despite the apparent overlap of anatomical targets, our behavioral tests of PCG projections to a set of selected targets indicated that the valence effects of PCG glutamatergic and GABAergic populations are mediated through distinguishable downstream effectors. The negative valence effect of PCG is achieved mainly through its glutamatergic projections to MD, VTA, LHA, MS/DB, and LPO (Figure S8C). The positive effect is through its GABAergic projections to VTA, LHA, and MS/DB (Figure S8C). Due to the large overlap of these targets, the local suppressive effect within PCG (Figure S6) can serve as a simple mechanism for producing opposite valence effects by the two PCG cell types, while the difference may reflect a difference in how negative and positive valence information is processed downstream of PCG. Although the aforementioned structures have all been shown to be associated with emotional processing in numerous studies,<sup>10,14,38,79,89–92</sup> particular attention is drawn to the VTA and LHA. Specifically, the activation of VTA dopaminergic neurons causes place preference,<sup>52</sup> and the suppression of VTA dopaminergic neurons by activating VTA GABAergic neurons leads to place aversion.<sup>57</sup> The activation of LHA GABAergic neurons promotes feeding and reward phenotypes,<sup>6</sup> whereas that of LHA glutamatergic neurons suppresses feeding and produces aversive behavioral phenotypes.<sup>7</sup> Based on these previous findings, we hypothesize that PCG glutamatergic and GABAergic axons can converge onto single VTA GABAergic neurons in a circuit configuration analogous to a so-called “opposing components” motif.<sup>3</sup> By opposingly regulating the activity of VTA dopaminergic neurons indirectly through the local GABAergic cells, they would be able to generate opposite behavioral effects: avoidance and preference, respectively. In our additional slice whole-cell recording experiment, we confirmed that individual VTA GABAergic neurons could receive both excitatory and inhibitory inputs from PCG (Figures S8A and S8B). Alternatively, via a “labeled lines” motif,<sup>3</sup> the PCG glutamatergic and GABAergic neurons may relay the negative and positive valence information in parallel to the next-stage glutamatergic and GABAergic neurons, respectively, e.g., in LHA and MS/DB, from where the valence information is further processed. It will be of great interest to further verify these hypothetical circuits in the PCG target structures in future studies. Interestingly, our results showed that the activation of PCG to PVT axons did not produce any obvious valence effect. This observation may be consistent with a recent study showing that PVT neurons encode stimulus salience irrespective of valence.<sup>93</sup>

In summary, our results reveal an important role of PCG in valence processing. Importantly, we show that both excitatory and inhibitory PCG neurons can drive motivated behavior, with opposite valences. By broadly receiving multisensory inputs of both aversive and rewarding nature, PCG processes and then broadcasts positive and negative valence information of sensory cues to an extended network critically involved in emotional/motivational processing.

## STAR★METHODS

Detailed methods are provided in the online version of this paper and include the following:

- KEY RESOURCES TABLE

- RESOURCE AVAILABILITY

- Lead contact
- Materials availability
- Data and code availability

- EXPERIMENTAL MODEL AND SUBJECT DETAILS

- METHOD DETAILS

- Abbreviation of mouse brain structures
- Viral injection
- Optogenetic manipulation
- Awake head-fixed animal preparation
- Sound generation
- Air puff stimulation
- Pharmacological silencing
- Optrode recording
- Intraoral infusion of sucrose water
- Fiber photometry recording
- Behavioral experiments
- Real-time animal detection and closed-loop optogenetic control
- RNAscope assay
- Slice recording
- Histology, imaging, and quantification

- QUANTIFICATION AND STATISTICAL ANALYSIS

- Data analysis
- Statistics

## SUPPLEMENTAL INFORMATION

Supplemental information can be found online at <https://doi.org/10.1016/j.neuron.2023.02.012>.

## ACKNOWLEDGMENTS

This work was supported by grants from the U.S. National Institutes of Health (R01DC008983, RF1MH114112, and MH116990 to L.I.Z.). H.W.T. was supported by NIH grants (EY019049 and MH116990), and I.R.W. was supported by NIH BRAIN Initiative awards RF1MH120017, U01MH114829, and U19MH114830.

## AUTHOR CONTRIBUTIONS

L.I.Z. and H.W.T. conceived the study and supervised the project. C.X. and J.W. carried out anatomical, *in vivo* recording, and all behavioral experiments as well as data analysis. G.Z. helped with behavioral experiments and data analysis. J.J.H. helped with anatomy. C.T. performed slice recording. L.S.

helped with recording data analysis. L.I.Z., H.W.T., and I.R.W. contributed to resources. C.X., L.I.Z., and H.W.T. wrote the manuscript.

## DECLARATION OF INTERESTS

I.R.W. is a consultant for Monosynaptix, LLC, advising on the design of neuroscientific experiments.

## INCLUSION AND DIVERSITY

We support inclusive, diverse, and equitable conduct of research.

Received: October 19, 2022

Revised: January 23, 2023

Accepted: February 7, 2023

Published: March 8, 2023

## REFERENCES

1. Etkin, A., Büchel, C., and Gross, J.J. (2015). The neural bases of emotion regulation. *Nat. Rev. Neurosci.* 16, 693–700. <https://doi.org/10.1038/nrn4044>.
2. LeDoux, J. (2012). Rethinking the emotional brain. *Neuron* 73, 653–676. <https://doi.org/10.1016/j.neuron.2012.02.004>.
3. Tye, K.M. (2018). Neural circuit motifs in valence processing. *Neuron* 100, 436–452. <https://doi.org/10.1016/j.neuron.2018.10.001>.
4. Berridge, K.C. (2019). Affective valence in the brain: modules or modes? *Nat. Rev. Neurosci.* 20, 225–234. <https://doi.org/10.1038/s41583-019-0122-8>.
5. Hu, H. (2016). Reward and aversion. *Annu. Rev. Neurosci.* 39, 297–324. <https://doi.org/10.1146/annurev-neuro-070815-014106>.
6. Jennings, J.H., Ung, R.L., Resendez, S.L., Stamatakis, A.M., Taylor, J.G., Huang, J., Veleta, K., Kantak, P.A., Aita, M., Shilling-Scrivo, K., et al. (2015). Visualizing hypothalamic network dynamics for appetitive and consummatory behaviors. *Cell* 160, 516–527. <https://doi.org/10.1016/j.cell.2014.12.026>.
7. Jennings, J.H., Rizzi, G., Stamatakis, A.M., Ung, R.L., and Stuber, G.D. (2013). The inhibitory circuit architecture of the lateral hypothalamus orchestrates feeding. *Science* 341, 1517–1521. <https://doi.org/10.1126/science.1241812>.
8. Baker, P.M., Jhou, T., Li, B., Matsumoto, M., Mizumori, S.J., Stephenson-Jones, M., and Vicentic, A. (2016). The lateral habenula circuitry: reward processing and cognitive control. *J. Neurosci.* 36, 11482–11488. <https://doi.org/10.1523/JNEUROSCI.2350-16.2016>.
9. Bromberg-Martin, E.S., Matsumoto, M., and Hikosaka, O. (2010). Dopamine in motivational control: rewarding, aversive, and alerting. *Neuron* 68, 815–834. <https://doi.org/10.1016/j.neuron.2010.11.022>.
10. Shen, L., Zhang, G.W., Tao, C., Seo, M.B., Zhang, N.K., Huang, J.J., Zhang, L.I., and Tao, H.W. (2022). A bottom-up reward pathway mediated by somatostatin neurons in the medial septum complex underlying appetitive learning. *Nat. Commun.* 13, 1194. <https://doi.org/10.1038/s41467-022-28854-z>.
11. Namburi, P., Al-Hasani, R., Calhoun, G.G., Bruchas, M.R., and Tye, K.M. (2016). Architectural representation of valence in the limbic system. *Neuropsychopharmacology* 41, 1697–1715. <https://doi.org/10.1038/npp.2015.358>.
12. Pignatelli, M., and Beyeler, A. (2019). Valence coding in amygdala circuits. *Curr. Opin. Behav. Sci.* 26, 97–106. <https://doi.org/10.1016/j.cobeha.2018.10.010>.
13. Zhang, X., Guan, W., Yang, T., Furlan, A., Xiao, X., Yu, K., An, X., Galbavy, W., Ramakrishnan, C., Deisseroth, K., et al. (2021). Genetically identified amygdala-striatal circuits for valence-specific behaviors. *Nat. Neurosci.* 24, 1586–1600. <https://doi.org/10.1038/s41593-021-00927-0>.

14. Cohen, J.Y., Haesler, S., Vong, L., Lowell, B.B., and Uchida, N. (2012). Neuron-type-specific signals for reward and punishment in the ventral tegmental area. *Nature* 482, 85–88. <https://doi.org/10.1038/nature10754>.
15. Hikosaka, O. (2010). The habenula: from stress evasion to value-based decision-making. *Nat. Rev. Neurosci.* 11, 503–513. <https://doi.org/10.1038/nrn2866>.
16. Matsumoto, M., and Hikosaka, O. (2007). Lateral habenula as a source of negative reward signals in dopamine neurons. *Nature* 447, 1111–1115. <https://doi.org/10.1038/nature05860>.
17. Hu, H., Cui, Y., and Yang, Y. (2020). Circuits and functions of the lateral habenula in health and in disease. *Nat. Rev. Neurosci.* 21, 277–295. <https://doi.org/10.1038/s41583-020-0292-4>.
18. Berridge, C.W., and Waterhouse, B.D. (2003). The locus coeruleus-noradrenergic system: modulation of behavioral state and state-dependent cognitive processes. *Brain Res. Brain Res. Rev.* 42, 33–84. [https://doi.org/10.1016/s0165-0173\(03\)00143-7](https://doi.org/10.1016/s0165-0173(03)00143-7).
19. Belova, M.A., Paton, J.J., and Salzman, C.D. (2008). Moment-to-moment tracking of state value in the amygdala. *J. Neurosci.* 28, 10023–10030. <https://doi.org/10.1523/JNEUROSCI.1400-08.2008>.
20. Paton, J.J., Belova, M.A., Morrison, S.E., and Salzman, C.D. (2006). The primate amygdala represents the positive and negative value of visual stimuli during learning. *Nature* 439, 865–870. <https://doi.org/10.1038/nature04490>.
21. Morrison, S.E., and Salzman, C.D. (2009). The convergence of information about rewarding and aversive stimuli in single neurons. *J. Neurosci.* 29, 11471–11483. <https://doi.org/10.1523/JNEUROSCI.1815-09.2009>.
22. Phelps, E.A., and LeDoux, J.E. (2005). Contributions of the amygdala to emotion processing: from animal models to human behavior. *Neuron* 48, 175–187. <https://doi.org/10.1016/j.neuron.2005.09.025>.
23. Etkin, A., Egner, T., and Kalisch, R. (2011). Emotional processing in anterior cingulate and medial prefrontal cortex. *Trends Cogn. Sci.* 15, 85–93. <https://doi.org/10.1016/j.tics.2010.11.004>.
24. Chikazoe, J., Lee, D.H., Kriegeskorte, N., and Anderson, A.K. (2014). Population coding of affect across stimuli, modalities and individuals. *Nat. Neurosci.* 17, 1114–1122. <https://doi.org/10.1038/nn.3749>.
25. Clithero, J.A., and Rangel, A. (2014). Informatic parcellation of the network involved in the computation of subjective value. *Soc. Cogn. Affect. Neurosci.* 9, 1289–1302. <https://doi.org/10.1093/scan/nst106>.
26. Cohen, J.Y., Amoroso, M.W., and Uchida, N. (2015). Serotonergic neurons signal reward and punishment on multiple timescales. *eLife* 4, e06346. <https://doi.org/10.7554/eLife.06346>.
27. Kim, J., Pignatelli, K.J., Xu, M., Itohara, S., and Tonegawa, S. (2016). Antagonistic negative and positive neurons of the basolateral amygdala. *Nat. Neurosci.* 19, 1636–1646.
28. Kravitz, A.V., Tye, L.D., and Kreitzer, A.C. (2012). Distinct roles for direct and indirect pathway striatal neurons in reinforcement. *Nat. Neurosci.* 15, 816–818. <https://doi.org/10.1038/nn.3100>.
29. Schultz, W., Dayan, P., and Montague, P.R. (1997). A neural substrate of prediction and reward. *Science* 275, 1593–1599. <https://doi.org/10.1126/science.275.5306.1593>.
30. Redondo, R.L., Kim, J., Arons, A.L., Ramirez, S., Liu, X., and Tonegawa, S. (2014). Bidirectional switch of the valence associated with a hippocampal contextual memory engram. *Nature* 513, 426–430. <https://doi.org/10.1038/nature13725>.
31. Lee, T.M.C., Wong, S.D., Shao, N.M.L., Men, R., Ge, W., So, J., Gao, K.F., Gao, J.H., and Chan, C.C. (2015). A pontine region is a neural correlate of the human affective processing network. *EBioMedicine* 2, 1799–1805. <https://doi.org/10.1016/j.ebiom.2015.10.020>.
32. Wong, J.J., Chang, D.H.F., Qi, D., Men, D., Gao, J.-H., and Lee, T.M.C. (2020). The pontine-driven somatic gaze tract contributes to affective processing in humans. *NeuroImage* 213, 116692. <https://doi.org/10.1016/j.neuroimage.2020.116692>.
33. Wong, J.J., Wong, N.M.L., Chang, D.H.F., Qi, D., Chen, L., and Lee, T.M.C. (2022). Amygdala–pons connectivity is hyperactive and associated with symptom severity in depression. *Commun. Biol.* 5, 574. <https://doi.org/10.1038/s42003-022-03463-0>.
34. Damasio, A.R., Grabowski, T.J., Bechara, A., Damasio, H., Ponto, L.L.B., Parvizi, J., and Hichwa, R.D. (2000). Subcortical and cortical brain activity during the feeling of self-generated emotions. *Nat. Neurosci.* 3, 1049–1056. <https://doi.org/10.1038/79871>.
35. Boucetta, S., Cissé, Y., Mainville, L., Morales, M., and Jones, B.E. (2014). Discharge profiles across the sleep-waking cycle of identified cholinergic, GABAergic, and glutamatergic neurons in the pontomesencephalic tegmentum of the rat. *J. Neurosci.* 34, 4708–4727. <https://doi.org/10.1523/JNEUROSCI.2617-13.2014>.
36. Cox, J., Pinto, L., and Dan, Y. (2016). Calcium imaging of sleep-wake related neuronal activity in the dorsal pons. *Nat. Commun.* 7, 10763. <https://doi.org/10.1038/ncomms10763>.
37. Zhang, G.-W., Sun, W.-J., Zingg, B., Shen, L., He, J., Xiong, Y., Tao, H.W., and Zhang, L.I. (2018). A non-canonical reticular-limbic central auditory pathway via medial septum contributes to fear conditioning. *Neuron* 97, 406–417.e4. <https://doi.org/10.1016/j.neuron.2017.12.010>.
38. Zhang, G.-W., Shen, L., Zhong, W., Zhang, Y., and Tao, H.W. (2018). Transforming sensory cues into aversive emotion via septal-habenular pathway. *Neuron* 99, 1016–1028.e5. <https://doi.org/10.1016/j.neuron.2018.07.023>.
39. Rahman, M., and Tadi, P. (2022). *Neuroanatomy, Pons* (StatPearls Publishing).
40. Abram, S.V., Hua, J.P.Y., and Ford, J.M. (2022). Consider the pons: bridging the gap on sensory prediction abnormalities in schizophrenia. *Trends Neurosci.* 45, 798–808. <https://doi.org/10.1016/j.tins.2022.08.008>.
41. Lecca, S., Meye, F.J., Trusel, M., Tchenio, A., Harris, J., Schwarz, M.K., Burdakov, D., Georges, F., and Mameli, M. (2017). Aversive stimuli drive hypothalamus-to-habenula excitation to promote escape behavior. *eLife* 6, 1–16. <https://doi.org/10.7554/eLife.30697>.
42. Stamatakis, A.M., and Stuber, G.D. (2012). Activation of lateral habenula inputs to the ventral midbrain promotes behavioral avoidance. *Nat. Neurosci.* 15, 1105–1107. <https://doi.org/10.1038/nn.3145>.
43. Gehrlach, D.A., Dolensek, N., Klein, A.S., Roy Chowdhury, R., Matthys, A., Junghänel, M., Gaitanos, T.N., Podgornik, A., Black, T.D., Reddy Vaka, N., et al. (2019). Aversive state processing in the posterior insular cortex. *Nat. Neurosci.* 22, 1424–1437. <https://doi.org/10.1038/s41593-019-0469-1>.
44. Liu, M.-Y., Yin, C.-Y., Zhu, L.-J., Zhu, X.-H., Xu, C., Luo, C.-X., Chen, H., Zhu, D.-Y., and Zhou, Q.-G. (2018). Sucrose preference test for measurement of stress-induced anhedonia in mice. *Nat. Protoc.* 13, 1686–1698. <https://doi.org/10.1038/s41596-018-0011-z>.
45. Belova, M.A., Paton, J.J., Morrison, S.E., and Salzman, C.D. (2007). Expectation modulates neural responses to pleasant and aversive stimuli in primate amygdala. *Neuron* 55, 970–984. <https://doi.org/10.1016/j.neuron.2007.08.004>.
46. Bradley, M.M., Miccoli, L., Escrig, M.A., and Lang, P.J. (2008). The pupil as a measure of emotional arousal and autonomic activation. *Psychophysiology* 45, 602–607. <https://doi.org/10.1111/j.1469-8986.2008.00654.x>.
47. Bradshaw, J. (1967). Pupil size as a measure of arousal during information processing. *Nature* 216, 515–516. <https://doi.org/10.1038/216515a0>.
48. Reimer, J., McGinley, M.J., Liu, Y., Rodenkirch, C., Wang, Q., McCormick, D.A., and Tolias, A.S. (2016). Pupil fluctuations track rapid changes in adrenergic and cholinergic activity in cortex. *Nat. Commun.* 7, 13289.
49. Wang, C.A., Boehnke, S.E., Itti, L., and Munoz, D.P. (2014). Transient pupil response is modulated by contrast-based saliency. *J. Neurosci.* 34, 408–417. <https://doi.org/10.1523/JNEUROSCI.3550-13.2014>.
50. Lu, L., Ren, Y., Yu, T., Liu, Z., Wang, S., Tan, L., Zeng, J., Feng, Q., Lin, R., Liu, Y., et al. (2020). Control of locomotor speed, arousal, and

- hippocampal theta rhythms by the nucleus incertus. *Nat. Commun.* 11, 262. <https://doi.org/10.1038/s41467-019-14116-y>.
51. Liao, H.I., Kidani, S., Yoneya, M., Kashino, M., and Furukawa, S. (2016). Correspondences among pupillary dilation response, subjective salience of sounds, and loudness. *Psychon. Bull. Rev.* 23, 412–425. <https://doi.org/10.3758/s13423-015-0898-0>.
  52. Tsai, H.C., Zhang, F., Adamantidis, A., Stuber, G.D., Bonci, A., de Lecea, L., and Deisseroth, K. (2009). Phasic firing in dopaminergic neurons is sufficient for behavioral conditioning. *Science* 324, 1080–1084. <https://doi.org/10.1126/science.1168878>.
  53. Zhang, F., Tsai, H.C., Airan, R.D., Stuber, G.D., Adamantidis, A.R., de Lecea, L., Bonci, A., and Deisseroth, K. (2015). Optogenetics in freely moving mammals: dopamine and reward. *Cold Spring Harb. Protoc.* 2015, 715–724. <https://doi.org/10.1101/pdb.top086330>.
  54. Li, Y., Zhong, W., Wang, D., Feng, Q., Liu, Z., Zhou, J., Jia, C., Hu, F., Zeng, J., Guo, Q., et al. (2016). Serotonin neurons in the dorsal raphe nucleus encode reward signals. *Nat. Commun.* 7, 10503. <https://doi.org/10.1038/ncomms10503>.
  55. Zhang, G.W., Shen, L., Tao, C., Jung, A.H., Peng, B., Li, Z., Zhang, L.I., and Tao, H.W. (2021). Medial preoptic area antagonistically mediates stress-induced anxiety and parental behavior. *Nat. Neurosci.* 24, 516–528. <https://doi.org/10.1038/s41593-020-00784-3>.
  56. Luo, L., Callaway, E.M., and Svoboda, K. (2018). Genetic dissection of neural circuits: a decade of progress. *Neuron* 98, 256–281. <https://doi.org/10.1016/j.neuron.2018.03.040>.
  57. Tan, K.R., Yvon, C., Turiault, M., Mirzabekov, J.J., Doehner, J., Labouèbe, G., Deisseroth, K., Tye, K.M., and Lüscher, C. (2012). GABA neurons of the VTA drive conditioned place aversion. *Neuron* 73, 1173–1183. <https://doi.org/10.1016/j.neuron.2012.02.015>.
  58. Iglesias, A.G., and Flagel, S.B. (2021). The paraventricular thalamus as a critical node of motivated behavior via the hypothalamic-thalamic-striatal circuit. *Front. Integr. Neurosci.* 15, 706713. <https://doi.org/10.3389/fnint.2021.706713>.
  59. Lavin, T.K., Jin, L., Lea, N.E., and Wickersham, I.R. (2020). Monosynaptic tracing success depends critically on helper virus concentrations. *Front. Synaptic Neurosci.* 12, 6. <https://doi.org/10.3389/fnsyn.2020.00006>.
  60. Liu, K., Kim, J., Kim, D.W., Zhang, Y.S., Bao, H., Denaxa, M., Lim, S.A., Kim, E., Liu, C., Wickersham, I.R., et al. (2017). Lhx6-positive GABA-releasing neurons of the zona incerta promote sleep. *Nature* 548, 582–587. <https://doi.org/10.1038/nature23663>.
  61. Weible, A.P., Schwarcz, L., Wickersham, I.R., Deblander, L., Wu, H., Callaway, E.M., Seung, H.S., and Kentros, C.G. (2010). Transgenic targeting of recombinant rabies virus reveals monosynaptic connectivity of specific neurons. *J. Neurosci.* 30, 16509–16513. <https://doi.org/10.1523/JNEUROSCI.2442-10.2010>.
  62. Rolls, E.T. (2000). The orbitofrontal cortex and reward. *Cereb. Cortex* 10, 284–294. <https://doi.org/10.1093/cercor/10.3.284>.
  63. Wallis, J.D. (2011). Cross-species studies of orbitofrontal cortex and value-based decision-making. *Nat. Neurosci.* 15, 13–19. <https://doi.org/10.1038/nn.2956>.
  64. Rolls, E.T., Cheng, W., and Feng, J. (2020). The orbitofrontal cortex: reward, emotion and depression. *Brain Commun.* 2, fcaa196. <https://doi.org/10.1093/braincomms/fcaa196>.
  65. Saez, A., Rigotti, M., Ostojic, S., Fusi, S., and Salzman, C.D. (2015). Abstract context representations in primate amygdala and prefrontal cortex. *Neuron* 87, 869–881. <https://doi.org/10.1016/j.neuron.2015.07.024>.
  66. McGaugh, J.L. (2004). The amygdala modulates the consolidation of memories of emotionally arousing experiences. *Annu. Rev. Neurosci.* 27, 1–28. <https://doi.org/10.1146/annurev.neuro.27.070203.144157>.
  67. Faget, L., Zell, V., Souter, E., McPherson, A., Ressler, R., Gutierrez-Reed, N., Yoo, J.H., Dulcis, D., and Hnasko, T.S. (2018). Opponent control of behavioral reinforcement by inhibitory and excitatory projections from the ventral pallidum. *Nat. Commun.* 9, 849. <https://doi.org/10.1038/s41467-018-03125-y>.
  68. Stephenson-Jones, M., Bravo-Rivera, C., Ahrens, S., Furlan, A., Xiao, X., Fernandes-Henriques, C., and Li, B. (2020). Opposing contributions of GABAergic and glutamatergic ventral pallidal neurons to motivational behaviors. *Neuron* 105, 921–933.e5. <https://doi.org/10.1016/j.neuron.2019.12.006>.
  69. Jennings, J.H., Sparta, D.R., Stamatakis, A.M., Ung, R.L., Pleil, K.E., Kash, T.L., and Stuber, G.D. (2013). Distinct extended amygdala circuits for divergent motivational states. *Nature* 496, 224–228. <https://doi.org/10.1038/nature12041>.
  70. Goto, M., Swanson, L.W., and Canteras, N.S. (2001). Connections of the nucleus incertus. *J. Comp. Neurol.* 438, 86–122. <https://doi.org/10.1002/cne.1303>.
  71. Yeomans, J.S., Li, L., Scott, B.W., and Frankland, P.W. (2002). Tactile, acoustic and vestibular systems sum to elicit the startle reflex. *Neurosci. Biobehav. Rev.* 26, 1–11. [https://doi.org/10.1016/s0149-7634\(01\)00057-4](https://doi.org/10.1016/s0149-7634(01)00057-4).
  72. Koch, M., and Schnitzler, H.U. (1997). The acoustic startle response in rat—circuits mediating evocation, inhibition and potentiation. *Behav. Brain Res.* 89, 35–49. [https://doi.org/10.1016/s0166-4328\(97\)02296-1](https://doi.org/10.1016/s0166-4328(97)02296-1).
  73. Protopopescu, X., Altemus, P.H., Tuescher, M., Polanecksky, M., McEwen, B., Silbersweig, D., and Stern, E. (2005). Orbitofrontal cortex activity related to emotional processing changes across the menstrual cycle. *Proc. Natl. Acad. Sci. USA* 102, 16060–16065. <https://doi.org/10.1073/pnas.0502818102>.
  74. Anderson, D.J., and Adolphs, R. (2014). A framework for studying emotions across species. *Cell* 157, 187–200. <https://doi.org/10.1016/j.cell.2014.03.003>.
  75. Wikenheiser, A.M., and Schoenbaum, G. (2016). Over the river, through the woods: cognitive maps in the hippocampus and orbitofrontal cortex. *Nat. Rev. Neurosci.* 17, 513–523. <https://doi.org/10.1038/nrn.2016.56>.
  76. McLaughlin, I., Dani, J.A., and De Biasi, M. (2017). The medial habenula and interpeduncular nucleus circuitry is critical in addiction, anxiety, and mood regulation. *J. Neurochem.* 142 (Suppl 2), 130–143. <https://doi.org/10.1111/jnc.14008>.
  77. Herkenham, M., and Nauta, W.J. (1979). Efferent connections of the habenular nuclei in the rat. *J. Comp. Neurol.* 187, 19–47. <https://doi.org/10.1002/cne.901870103>.
  78. Hikosaka, O., Sesack, S.R., Lecourtier, L., and Shepard, P.D. (2008). Habenula: crossroad between the basal ganglia and the limbic system. *J. Neurosci.* 28, 11825–11829. <https://doi.org/10.1523/JNEUROSCI.3463-08.2008>.
  79. McGovern, D.J., Polter, A.M., and Root, D.H. (2021). Neurochemical signaling of reward and aversion to ventral tegmental area glutamate neurons. *J. Neurosci.* 41, 5471–5486. <https://doi.org/10.1523/JNEUROSCI.1419-20.2021>.
  80. Ouahaz, Z., Fleming, H., and Mitchell, A.S. (2018). Cognitive functions and neurodevelopmental disorders involving the prefrontal cortex and mediodorsal thalamus. *Front. Neurosci.* 12, 33. <https://doi.org/10.3389/fnins.2018.00033>.
  81. Collins, D.P., Anastasiades, P.G., Marlin, J.J., and Carter, A.G. (2018). Reciprocal circuits linking the prefrontal cortex with dorsal and ventral thalamic nuclei. *Neuron* 98, 366–379.e4. <https://doi.org/10.1016/j.neuron.2018.03.024>.
  82. Oddie, S.D., and Bland, B.H. (1998). Hippocampal formation theta activity and movement selection. *Neurosci. Biobehav. Rev.* 22, 221–231. [https://doi.org/10.1016/s0149-7634\(97\)00003-1](https://doi.org/10.1016/s0149-7634(97)00003-1).
  83. Müller, C., and Remy, S. (2018). Septo-hippocampal interaction. *Cell Tissue Res.* 373, 565–575. <https://doi.org/10.1007/s00441-017-2745-2>.
  84. Vann, S.D., and Nelson, A.J.D. (2015). The mammillary bodies and memory: more than a hippocampal relay. *Prog. Brain Res.* 219, 163–185. <https://doi.org/10.1016/bs.pbr.2015.03.006>.

85. Roseberry, T.K., Lee, A.M., Lalive, A.L., Wilbrecht, L., Bonci, A., and Kreitzer, A.C. (2016). Cell-type-specific control of brainstem locomotor circuits by basal ganglia. *Cell* 164, 526–537. <https://doi.org/10.1016/j.cell.2015.12.037>.
86. Andrade, T.G., Zangrossi, H.J., and Graeff, F.G. (2013). The median raphe nucleus in anxiety revisited. *J. Psychopharmacol.* 27, 1107–1115. <https://doi.org/10.1177/0269881113499208>.
87. Szőnyi, A., Zichó, K., Barth, A.M., Gönczi, R.T., Schlingloff, D., Török, B., Sipos, E., Major, A., Bardóczi, Z., Sos, K.E., et al. (2019). Median raphe controls acquisition of negative experience in the mouse. *Science* 366, eaay8746.
88. Wang, D.V., Yau, H.-J., Broker, C.J., Tsou, J.-H., Bonci, J.H., and Ikemoto, S. (2015). Mesopontine median raphe regulates hippocampal ripple oscillation and memory consolidation. *Nat. Neurosci.* 18, 728–735.
89. Lazaridis, I., Tzortzi, O., Weglage, M., Märtin, A., Xuan, Y., Parent, M., Johansson, Y., Fuzik, J., Fürth, D., Fenno, L.E., et al. (2019). A hypothalamus-habenula circuit controls aversion. *Mol. Psychiatry* 24, 1351–1368. <https://doi.org/10.1038/s41380-019-0369-5>.
90. Barker, D.J., Miranda-Barrientos, J., Zhang, S., Root, D.H., Wang, H.L., Liu, B., Calipari, E.S., and Morales, M. (2017). Lateral preoptic control of the lateral habenula through convergent glutamate and GABA transmission. *Cell Rep.* 21, 1757–1769. <https://doi.org/10.1016/j.celrep.2017.10.066>.
91. Root, D.H., Estrin, D.J., and Morales, M. (2018). Aversion or salience signaling by ventral tegmental area glutamate neurons. *iScience* 2, 51–62. <https://doi.org/10.1016/j.isci.2018.03.008>.
92. Matsumoto, H., Tian, J., Uchida, N., and Watabe-Uchida, M. (2016). Midbrain dopamine neurons signal aversion in a reward-context-dependent manner. *eLife* 5, e17328. <https://doi.org/10.7554/eLife.17328>.
93. Zhu, Y., Nachtrab, G., Keyes, P.C., Allen, W.E., Luo, L., and Chen, X. (2018). Dynamic salience processing in paraventricular thalamus gates associative learning. *Science* 362, 423–429. <https://doi.org/10.1126/science.aat0481>.
94. Oh, S.W., Harris, J.A., Ng, L., Winslow, B., Cain, N., Mihalas, S., Wang, Q., Lau, C., Kuan, L., Henry, A.M., et al. (2014). A mesoscale connectome of the mouse brain. *Nature* 508, 207–214. <https://doi.org/10.1038/nature13186>.
95. Han, X., Chow, B.Y., Zhou, H., Klapoetke, N.C., Chuong, A., Rajimehr, R., Yang, A., Baratta, M.V., Winkle, J., Desimone, R., et al. (2011). A high-light sensitivity optical neural silencer: development and application to optogenetic control of non-human primate cortex. *Front. Syst. Neurosci.* 5, 18. <https://doi.org/10.3389/fnsys.2011.00018>.
96. Grdinaru, V., Zhang, F., Ramakrishnan, C., Mattis, J., Prakash, R., Diester, I., Goshen, I., Thompson, K.R., and Deisseroth, K. (2010). Molecular and cellular approaches for diversifying and extending optogenetics. *Cell* 141, 154–165. <https://doi.org/10.1016/j.cell.2010.02.037>.
97. Chen, T.W., Wardill, T.J., Sun, Y., Pulver, S.R., Renninger, S.L., Baohan, A., Schreiter, E.R., Kerr, R.A., Orger, M.B., Jayaraman, V., et al. (2013). Ultrasensitive fluorescent proteins for imaging neuronal activity. *Nature* 499, 295–300. <https://doi.org/10.1038/nature12354>.
98. Dong, H.W. (2008). *The Allen Reference Atlas: A Digital Color Brain Atlas of the C57BL/6J Male Mouse* (John Wiley and Sons).
99. Zingg, B., Chou, X.-L., Zhang, Z.G., Mesik, L., Liang, F., Tao, H.W., and Zhang, L.I. (2017). AAV-mediated anterograde transsynaptic tagging: mapping corticocollicular input-defined neural pathways for defense behaviors. *Neuron* 93, 33–47. <https://doi.org/10.1016/j.neuron.2016.11.045>.
100. Zingg, B., Peng, B., Huang, J., Tao, H.W., and Zhang, L.I. (2020). Synaptic specificity and application of anterograde transsynaptic AAV for probing neural circuitry. *J. Neurosci.* 40, 3250–3267. <https://doi.org/10.1523/JNEUROSCI.2158-19.2020>.
101. Zingg, B., Dong, H.W., Tao, H.W., and Zhang, L.I. (2022). Application of AAV1 for anterograde transsynaptic circuit mapping and input-dependent neuronal cataloging. *Curr. Protoc.* 2, e339. <https://doi.org/10.1002/cpz1.339>.
102. Chou, X.-L., Wang, X., Zhang, Z.-G., Shen, L., Zingg, B., Huang, J., Zhong, W., Mesik, W., Zhang, L.I., and Tao, H.W. (2018). Inhibitory gain modulation of defense behaviors by zona incerta. *Nat. Commun.* 9, 1151. <https://doi.org/10.1038/s41467-018-03581-6>.
103. Chou, X.-L., Fang, Q., Yan, L., Zhong, W., Peng, B., Li, H., Wei, J., Tao, H.W., and Zhang, L.I. (2020). Contextual and cross-modality modulation of auditory cortical processing through pulvinar mediated suppression. *eLife* 9, e54157.
104. Fang, Q., Chou, X.-L., Peng, B., Zhong, W., Zhang, L.I., and Tao, H.W. (2020). A differential circuit via retino-colliculo-pulvinar pathway enhances feature selectivity in visual cortex through surround suppression. *Neuron* 105, 355–369.e6. <https://doi.org/10.1016/j.neuron.2019.10.027>.
105. Xiong, L.F., Zingg, X.R., Ji, B., Zhang, X.Y., Zhang, L.I., and Tao, H.W. (2015). Sensory cortical control of a visually induced arrest behavior via corticotectal projections. *Neuron* 86, 755–767. <https://doi.org/10.1016/j.neuron.2015.03.048>.
106. Vinck, M., Batista-Brito, R., Knoblich, U., and Cardin, J.A. (2015). Arousal and locomotion make distinct contributions to cortical activity patterns and visual encoding. *Neuron* 86, 740–754. <https://doi.org/10.1016/j.neuron.2015.03.028>.
107. Hintiryan, H., Hayes, U.L., and Chambers, K.C. (2006). Intraoral cheek fistulae: a refined technique. *Lab Anim.* 40, 456–464. <https://doi.org/10.1258/002367706778476479>.
108. Zhang, G.-W., Shen, L., Li, Z., Tao, H.W., and Zhang, L.I. (2019). Track-Control, an automatic video-based real-time closed-loop behavioral control toolbox. Preprint at bioRxiv. <https://doi.org/10.1101/2019.12.11.873372>.
109. Li, Z., Wei, J.-X., Zhang, G.-W., Huang, J.J., Zingg, B., Wang, X., Tao, H.W., and Zhang, L.I. (2021). Corticostriatal control of defense behavior in mice induced by auditory looming cues. *Nat. Commun.* 12, 1–13. <https://doi.org/10.1038/s41467-021-21248-7>.

## STAR★METHODS

## KEY RESOURCES TABLE

REAGENT or RESOURCE	SOURCE	IDENTIFIER
<b>Antibodies</b>		
Fluorescent Nissl Stain	Invitrogen	RRID: AB_2572212
<b>Bacterial and Virus Strains</b>		
AAV1-CAG-FLEX-GFP-WPRE	A gift from Hongkui Zeng <sup>94</sup>	Addgene plasmid # 51502; RRID:Addgene_51502
AAV1-EF1a-DIO-hChR2-eYFP	A gift from Karl Deisseroth	Addgene plasmid # 20298; RRID:Addgene_20298
AAV1-EF1a-DIO-eYFP	A gift from Karl Deisseroth	Addgene plasmid # 27056; RRID:Addgene_27056
AAV1-CAG-FLEX-ArchT-GFP	A gift from Edward Boyden <sup>95</sup>	Addgene plasmid # 29777; RRID:Addgene_29777
pAAV-hSyn-hChR2 (H134R)-eYFP	A gift from Karl Deisseroth	Addgene plasmid # 26973; RRID:Addgene_26973
pAAV-TREtight-mTagBFP2-B19G	A gift from Ian Wickersham <sup>60</sup>	Addgene plasmid # 100799; RRID:Addgene_100799
pAAV-Syn-FLEX-splitTVA-EGFP-tTA	A gift from Ian Wickersham <sup>60</sup>	Addgene plasmid # 100798; RRID:Addgene_100798
RVΔG-4mCherry (EnVA)	A gift from Ian Wickersham	N/A
pAAV-Ef1a-DIO-eNpHR-3.0-EYFP	A gift from Karl Deisseroth <sup>96</sup>	Addgene plasmid # 26966; RRID:Addgene_26966
AAV1-Syn-FLEX-GCamp6s-WPRE-SV40	A gift from Douglas Kim & GENIE Project <sup>97</sup>	Addgene plasmid # 100845; RRID:Addgene_100845
<b>Chemicals, peptides, and recombinant proteins</b>		
Kwik-Cast Sealant	WPI, Inc.	KWIK-CAST
Paraformaldehyde	Alfa Aesar OmniPur	10194340
NaCl	OmniPur	UI27FZEMS
KCl	Mallinckrodt	7447-40-7
NaHCO3	EMD Chemicals	48204847
MgCl2	J.T. Baker	7791-18-6
CaCl2	EMD Chemicals	41046444
Glucose	Sigma	SLBC6575V
Sucrose	Millipore	D00168514
Agarose	OmniPur	3332C511
DAPI	ACDbio	323108
Dil	Invitrogen	D282
Muscimol,>98%; Tocris; 10mg	Fisher Scientific	28910
<b>Experimental models: Organisms/strains</b>		
Mouse: C57BL/6J	The Jackson Laboratory	RRID: IMSR_JAX:000664
Mouse: Ai14	The Jackson Laboratory	RRID: IMSR_JAX:007914
Mouse: VGlutT2-ires-Cre mice	The Jackson Laboratory	RRID: IMSR_JAX: 016963
Mouse: VGAT-ires-Cre mice	The Jackson Laboratory	RRID: IMSR_JAX: 016962
<b>Oligonucleotides</b>		
RNAscope Probe-Mm-Slc17a6	Advanced Cell Diagnostics	Cat# 319171-C2
RNAscope Probe-Mm-Slc32a1	Advanced Cell Diagnostics	Cat# 319191-C3
<b>Software and algorithms</b>		
Data acquisition with Labview	LabVIEW	<a href="http://www.ni.com/en-us/shop/labview.html">http://www.ni.com/en-us/shop/labview.html</a> ; RRID: SCR_014325
Custom-written MATLAB code for analysis	MATLAB	<a href="http://www.mathworks.com/">http://www.mathworks.com/</a> ; RRID: SCR_001622
Allen Reference Atlas	Dong <sup>98</sup>	<a href="http://www.brainmap.org/">http://www.brainmap.org/</a> ; RRID: SCR_008848

(Continued on next page)

**Continued**

REAGENT or RESOURCE	SOURCE	IDENTIFIER
Offline sorter	Plexon	<a href="http://plexon.com/">http://plexon.com/</a> ; RRID: SCR_000012
Prism	GraphPad	<a href="https://www.graphpad.com/scientific-software/prism/">https://www.graphpad.com/scientific-software/prism/</a> ; RRID:SCR_002798
Custom-written python code for analysis	Python	<a href="https://www.python.org/">https://www.python.org/</a> ; RRID:SCR_008394
OpenCV library	OpenCV	<a href="https://opencv.org/">https://opencv.org/</a> ; RRID: SCR_015526
Fiji	NIH	<a href="https://fiji.sc/">https://fiji.sc/</a> ; RRID:SCR_002285
Original code for analysis of behavioral data	<a href="https://doi.org/10.5281/zenodo.7604169">https://doi.org/10.5281/zenodo.7604169</a>	<a href="https://doi.org/10.5281/zenodo.7604169">https://doi.org/10.5281/zenodo.7604169</a>
<b>Other</b>		
Free Field Speaker	TDT MF1	N/A
Sound-Attenuation Booth	Gretch-Ken Industries	N/A
NI board for sound generation	National Instrument	PCI-6731
Microvalve	Lee Co.	LFAA1209512H
Optrode	Neuronexus Technologies	A1x16-Poly2-5mm-50 s-177-OA16LP

**RESOURCE AVAILABILITY****Lead contact**

Further information and requests for resources and reagents should be directed to and will be fulfilled by the Lead Contact, Li I. Zhang ([liizhang@usc.edu](mailto:liizhang@usc.edu)).

**Materials availability**

This study did not generate new unique reagents.

**Data and code availability**

- All data reported in this paper will be shared by the [lead contact](#) upon request.
- All original code has been deposited at Zenodo and is publicly available as of the date of publication. DOIs are listed in the [key resources table](#).
- Any additional information required to reanalyze the data reported in this paper is available upon request.

**EXPERIMENTAL MODEL AND SUBJECT DETAILS**

All experimental procedures in this study were in accordance with the guidelines for the care and use of laboratory animals of the US National Institutes of Health (NIH), and were approved by Animal Care and Use Committee (IACUC) of the University of Southern California. Experiments were performed in adult (2–4 months old) male and female mice. The Vglut2-ires-Cre (stock # 016963), Vgat-ires-Cre (stock # 016962), Ai14 (Cre-dependent tdTomato reporter line; stock # 007914) and C57BL/6J (stock # 000664) mice were obtained from the Jackson Laboratory and were housed with a 12 h light-dark cycle, at 18–23°C temperature and 40–60% humidity. All recordings and behavioral tests were conducted in the dark cycle.

**METHOD DETAILS****Abbreviation of mouse brain structures**

All mouse brain structures in this study are referenced to the Allen Brain Atlases (<https://atlas.brain-map.org>). ARH, arcuate hypothalamic nucleus; BST, bed nuclei of the stria terminalis; CNU, cerebral nuclei; CTX, cerebral cortex; CB, cerebellum; CUN, cuneiform nucleus; CS, superior central nucleus raphe; DMH, dorsomedial nucleus of the hypothalamus; DR, dorsal nucleus raphe; DTN, dorsal tegmental nucleus; DB, diagonal band nucleus; fr, fasciculus retroflexus; HPF, hippocampal formation; HY, hypothalamus; IMD, intermediodorsal nucleus of the thalamus; IPN, interpeduncular nucleus; IF, interfascicular nucleus raphe; ICe, external cortex of the inferior colliculus; LH, lateral habenula; LS, lateral septal nucleus; LPO, lateral preoptic area; LHA, lateral hypothalamic area; MOB,

main olfactory bulb; MB, midbrain; MY, medulla; MH, medial habenula; MD, mediodorsal nucleus of the thalamus; MS/DB, medial septum and diagonal band nucleus; MPN, medial preoptic nucleus; MOs, second motor area; MA, magnocellular nucleus; MPO, medial preoptic area; MM, medial mammillary nucleus; OFC, orbitofrontal cortex; OT, olfactory tubercle; PVT, paraventricular nucleus of the thalamus; PAG, periaqueductal gray; PG, pontine gray; PCG, pontine central gray; PRN, pontine reticular nucleus; PL, prelimbic area; P, pons; RSP, retrosplenial cortex; SOC, superior olive complex; SC, superior colliculus; SI, substantia innominate; SuM, supramammillary nucleus; SNr, substantia nigra reticular part; TH, thalamus; VTA, ventral tegmental area; VMH, ventro-medial hypothalamic nucleus; VM, ventral medial nucleus of the thalamus; ZI, zona incerta.

### Viral injection

AAV1-CAG-FLEX-GFP-WPRE (Addgene, 51502), AAV1-EF1 $\alpha$ -DIO-hChR2 (H134R)-EYFP-WPRE (Addgene, 20298), AAV1-Ef1a-DIO-eNpHR 3.0-EYFP (Addgene, 26966), AAV1-hSyn-hChR2 (H134R)-EYFP (Addgene, 26973), AAV1-EF1a-DIO-eYFP-WPRE (Addgene, 27056), AAV1-CAG-FLEX-ArchT-GFP (Addgene, 29777), AAV1-Syn-FLEX-GCaMP6s-WPRE-SV4 (Addgene, 100845), AAV1-Syn-FLEX-TVA-EGFP-tTA (Addgene, 100798), AAV1-TREtight-mTagBFP2-B19G (Addgene, 100799),<sup>59,60</sup> RVΔG-4mCherry (EnvA)<sup>61</sup> were used in this study. Stereotaxic injection of viruses was conducted as we previously described.<sup>99–101</sup> Mice were placed on a heating pad and were anesthetized with 1.5% isoflurane (in oxygen) by inhalation during the whole surgery procedure. Buprenorphine was injected subcutaneously after anesthesia. After asepsis, a small incision was made on the skin and the muscles were slightly removed to expose the skull. For virus injection, a 0.2 mm craniotomy window was made for the target region (PCG, AP –5.5 mm, ML +0.4 mm, DV –3.2 mm). Stereotaxic coordinates of injection were based on the Allen Reference Atlas [www.brain-map.org](http://www.brain-map.org). For pressure injection, the virus was delivered through a pulled glass micropipette with beveled tip (~20  $\mu$ m diameter) via a micropump (World Precision Instruments). The volume for each injection was 50 nl and injected at a rate of 15 nl/min. For iontophoresis injection, 3  $\mu$ A current was applied (7 sec on, 7 sec off cycle) for 5 min. The pipette was allowed to rest at the injection site for 5 min before being withdrawn slowly. The scalp was then sutured. After the surgery, antibiotic ointment was applied to the surgery wound before returning the animals to their home cages. Ketoprofen (0.5 mg/kg) was applied for three days following all the surgeries. Viruses were expressed for at least 3 weeks before behavioral, tracing or recording experiments. After each experiment, the brain was sectioned and automatically imaged under a confocal microscope to confirm viral expression. To trace the monosynaptic input to Vglut2+ or Vgat+ neurons in PCG, AAV1-Syn-FLEX-TVA-EGFP-tTA and AAV1-TREtight-mTagBFP2-B19G were mixed (1:1) and stereotactically injected into PCG of Vglut2-Cre or Vgat-Cre mice, after one week, RVΔG-4mCherry (EnvA) was injected at the same site.

### Optogenetic manipulation

For optogenetic manipulations, optical fibers were implanted into the targeted region two weeks after the virus injection (PCG, bilateral implantation, AP –5.5 mm, ML +1.75 mm, DV –3.1 mm, with a 15° angle; MD, bilateral implantation, AP –1.2 mm, ML +1.5 mm, DV –3.0 mm, with a 15° angle; PVT, unilateral implantation, AP –1.2 mm, ML +0.6 mm, DV –2.7 mm; with a 10° angle; LHA, bilateral implantation, AP –1.5 mm, ML +1.2 mm, DV –4.7 mm, with a 10° angle; LPO, bilateral implantation, AP +0.2 mm, ML +1.2 mm, DV –4.5 mm, with a 10° angle; VTA, AP –3.2 mm, ML +1.5mm, DV –4.3 mm, with 11° angle; MS, unilateral implantation, AP +0.85 mm, ML +0.5 mm, DV –3.6 mm, with a 10° angle;). Animals were anesthetized with 1.5% isoflurane and a small hole was drilled. The optic cannulas (200  $\mu$ m core, NA=0.22, RWD Inc.) were lowered into the targeted depth and was fixed with dental cement. A metal screw for head fixation was mounted on the top of the skull for animal pupil size tests. After surgery, the animals were allowed to recover for at least 3 days before the experiments. Before any behavioral tests, mice were connected to optical cables without LED stimulation for habituation for three days. To block the light leak, a black tape wrapped around the connection between optical cable and implanted ferrule. For all the optogenetic activation experiments, the blue LED source (470 nm, 20 Hz, 5-ms duration, Thorlabs) was used. For the optogenetic silencing experiments, the green (530 nm, Thorlabs) or yellow light (589 nm, Thorlabs) was delivered continuously. All light was delivered at about 7–10 mW (measured from the fiber tip). For noise or air puff-induced place aversion test combined with optogenetic inhibition, green LED light and 80 dB SPL noise or air puff were delivered simultaneously. For stimulation of PCG projections in different target regions, 100 nL muscimol (0.7 mM in ACSF with 5% DMSO) was applied to the PCG via a pipette connected to a microinjector before behavioral tests to silence PCG neurons. All the control groups received the same experiment procedures and light stimulation. After each experiment, animals were transcardially perfused and examined the location of the viral expression and the track of optical fibers.

### Awake head-fixed animal preparation

For awake recording from head-fixed animal preparations, the procedures were similar as previously described.<sup>37,102–105</sup> Mice were placed on a heating pad and anesthetized with 1.5% isoflurane, and a screw for head fixation was mounted on top of the skull with dental cement. One day before the recording, a craniotomy window was made over the recording region (PCG: AP –5.4 – –5.7 mm, ML +0.4 mm, DV –3.1 – –3.5 mm). Silicone adhesive (Kwik-Cast Sealant, WPI Inc.) was applied to cover the craniotomy window until the recording sessions. Animals were allowed to recover for one week before all the recording experiments. Mice were trained to run freely on a rotatable plate during the recovery period.

**Sound generation**

The sound stimulation and data acquisition were generated by custom-written software in LabVIEW (PCI-6731 NI board for sound generation, 16-bits output, 1MHz sampling rate, National Instruments, Austin, TX). For in vivo head-fixed recording, broadband white noise (100-ms duration, 50 trials, with-5-s inter-stimulus interval) at 70 dB SPL were applied. An open field speaker (MF1, Tucker-Davis Technologies) was placed to the contralateral side and 10 cm away from the ear. For noise-induced pupil dilation test, 70 dB SPL white noise (3-s duration, 30 trials, 30-s inter-stimulus interval) were used. For noise-induced place aversion test, 80 dB SPL white noise was continuously delivered through a speaker which was placed in a corner of the designated stimulation chamber whenever the mouse entered that chamber.

**Air puff stimulation**

The air puffs were generated by the center air with an internal pressure of around 40-55 psi. A microvalve (LFAA1209512H, Lee Co, ESSEX, CT) was used to deliver and control the intensity of the air puff. For in vivo awake mice recording, air puffs were delivered to the back of the mouse with minimum waiting intervals of 60 s. For air puff induced place aversion, a battery powered fan was used to deliver the continuous wind blow in the designated stimulation chamber. For air puff induced pupil size change, we followed previous methods,<sup>50,106</sup> a small tube was positioned behind the mice's back and air puffs (3-s duration, 30 trials, with 60 s inter-stimulus interval) were delivered to the body of the mouse in the head-fixed mice.

**Pharmacological silencing**

For pharmacological silencing of PCG, mice underwent a drug cannula implantation surgery one week before the pharmacological manipulation. Surgery procedure was similar to optical fiber implantation as described above. Mice were anesthetized with isoflurane and a drug cannula (internal diameter: 140  $\mu\text{m}$ ) was implanted bilaterally into the PCG. Fluorescent muscimol-bodipy (0.7 mM in ACSF with 5% DMSO) or saline was infused via the implanted cannula ten minutes before behavioral tests. A thin pipette connected with a microinjector for drug injection was inserted through the implanted drug cannula, and muscimol (100 nL, per hemisphere) was slowly perfused into the PCG bilaterally. The mouse was perfused transcardially to examine the location of cannula and drug spread after the experiments.

**Optrode recording**

All the in vivo recordings were performed in a sound-attenuation room (Acoustic Systems) as previously described.<sup>37,38</sup> Silicon seal was removed, then a 16-channel silicon probe (NeuroNexus Technologies) was lowered into the target brain structure. To identify glutamatergic or GABAergic neurons in the PCG, an optrode (A1x16-Poly2-5mm-50 s-177-OA16LP, 16 contacts separated by 50  $\mu\text{m}$ , the distance between the tip of the optic fiber and the probes is 200  $\mu\text{m}$ , NA 0.22, NeuroNexus Technologies) connected to a LED light source (470 nm, Thorlabs) via an optic fiber was lowered into the target brain structure. To identify ChR2+ neurons, 16-Hz (5-ms pulse duration, controlled via an Arduino microcontroller) LED pulse trains were delivered intermittently. All signals were recorded and saved for offline analysis. The silicone probe was coated with Dil (Invitrogen) to label the electrode track.

**Intraoral infusion of sucrose water**

An intraoral cheek fistula surgery was performed following previous studies.<sup>54,107</sup> Briefly, a soft silastic tubing was subcutaneously inserted to the oral cavity of the mouse through a small incision on cheek. The tube was adhesive to the cheek with sutures. This approach allowed us to precisely control the time and volume of sucrose or water delivered into the mouth. For passive sucrose water delivery, the mouse was water deprived for 12 h. After recovery from the surgery, a micro pump (Lee-Company) was used to infuse sucrose water (5% w/v, with 30 s intervals) into the oral cavity through the tube. A custom-written LabVIEW program was used to serve as a trigger signal for each trial.

**Fiber photometry recording**

To obtain calcium signals, 480 nm LED light (Thorlabs) was bandpass filtered (ET470/24M, Chroma), focused by an objective lens (Olympus), and coupled through an optical fiber (O.D.= 400  $\mu\text{m}$ , NA = 0.48, 1 m long, Doric) connected to an implanted optic fiber (400  $\mu\text{m}$ , NA = 0.5, Thorlabs) via a ceramic sleeve. The LED power was set at 0.02 mW at the tip of the optical fiber. At this power, no significant photobleaching was observed. The fluorescence calcium signal was bandpass filtered (ET525/36M, Chroma) and collected by a photomultiplier tube (H11706-40, Hamamatsu), and then passed through an amplifier (Model SR570, Stanford Research System) and low-pass filtered (30 Hz). Then the current output was converted to a voltage signal by a data acquisition card (PCI-MIO-16E-4, National Instruments). The photometry voltage signals were digitized at 250 Hz and recorded by LabView software. Data were obtained using custom LabVIEW software and off-line analyzed using custom MATLAB software. No movement-related artifact has been detected in our system.

**Behavioral experiments**

All behavior tests were conducted in a sound-attenuation booth (Acoustic Systems) during the dark cycle of the mice. All the behavioral videos were recorded and saved for further offline analysis.

**Real-time place preference test**

We carried out the RTPP test following our previous studies.<sup>38</sup> Mouse implanted with optic fibers was placed in a white plastic box (40 cm × 20 cm × 20 cm) with two compartments. The mouse could freely explore between the two compartments through a small opening. For each test session, the mouse was first put into the non-stimulation (randomly assigned) chamber. Whenever the mouse entered the other chamber, 470 nm blue LED (20 Hz, with 5-ms duration) or 530 nm green LED (continuous stimulation) was delivered until the animal exited. The total duration of each session was 20 min. After each session, the chamber was cleaned with 70% alcohol.

**Conditioned place aversion or preference test**

A clear acrylic behavior box (50 cm × 25 cm × 25 cm) was divided into three chambers. The three chambers were separated by a corridor and have distinct walls drawings, floor, and shape.

The middle chamber has a grey smooth metal plate floor, the left chamber has black and white stripes on the walls and a grid-wire floor, and the right chamber has black and white squares on the walls and a parallel-wire floor. On day 1 (pre-conditioning day), mice freely explored the chambers for 20 min without light. On the 2nd and 3rd day (conditioning days), mice were confined to one of two sides and received either no stimulation or photostimulation (20 Hz, 5 ms pulse duration) for 20-minute periods in the morning and afternoon, respectively. The stimulation chamber was assigned randomly to the animal. On the 4th day (test day), the animal was placed in the middle chamber and could freely get access to all chambers for 20 min.

**Pupil diameter tracking and offline quantification**

For pupil monitoring, the mouse head was fixed using a previously implanted head screw and the mouse body was restricted within a rectangle barrel. The mouse eye was illuminated by an infrared LED light source (LIU780A, Thorlabs) and a camera was used to monitor the left or right eye of the mouse and the video of eye images was acquired by Fly Capture2 software. For PCG activation or terminal activation experiments, blue LED (20 Hz, 5-ms pulse duration, 30-trials, with 30-s inter-stimulus interval) was applied bilaterally. For PCG inhibition combined with sensory stimuli, bilateral green LED was applied continuously, and sensory stimulation was presented for 3-s after 2-s of the baseline activity. The total recording duration of each trial was 10-s. The pupil size was analyzed offline with Python 3.4: each frame was Gaussian filtered and the black pupil was extracted using a threshold adjusted for each experiment. A few frames were dropped due to the eye blink and the corresponding pupil size value was estimated using interpolation based on 5 frames before and after the eye blink.<sup>55</sup> For pupil diameter analysis, the baseline was defined as a period of 2-s before LED or sensory stimulation onset. We then calculated the change in pupil size by averaging for a period of 2 to 5-s following the onset of the stimulus, then the peak amplitude of pupil size during the stimulation was calculated and normalized. Trials without LED or sensory stimuli were used as the control to evaluate the spontaneous fluctuations of pupil size.

**Open field test**

Mice were placed in a white plastic test box (60 cm × 60 cm × 30 cm) to test the baseline locomotion activity. They were allowed to move freely to habituate for 5–10 min. Each animal was tested for 1 session per day and each session lasted 16 min, during which blue LED stimulation (20 Hz, duration 60-s, with a 180-s inter-stimulus interval) was applied. The animal's movement track was recorded by an overhead camera.

**Food intake test**

Food intake test was performed in a white plastic box (40 cm × 20 cm × 20 cm) with two compartments. Mice were housed with food and water ad libitum. Before the behavioral test, the animal was food deprived for 24 h with water ad libitum. The mouse was first put into the non-stimulation (randomly assigned) chamber, whenever the mouse entered the other chamber, blue LED stimulation (20 Hz, 5-ms duration) was continuously applied until the animal exited. Standard grain pellets were used as the food sources and put it in the corner of LED-stimulated chamber. The total duration of each session was 20 min. The weight of food consumed was measured after the test block.

**Sucrose preference test**

Mice were first trained for 30 min daily over 5 d to consume either a sucrose solution or only water, from two sipper tubes presented in a custom-built chamber, until they reached a stable preference for sucrose. Animals were water deprived for 24 h before the test and then exposed to one bottle of 2% sucrose water and one bottle of pure water for 1 h. Bottle positions were switched after 30 min. For ArchT-expressing mice, a green LED source (530 nm, constant illumination) were delivered for 1 h. The sucrose preference index was calculated as (sucrose consumption – water consumption) / (sucrose consumption + water consumption).

**Foot shocks**

Animals were placed into an acrylic box (25 cm × 25 cm × 30 cm) with metal grid floor. The foot shocks (0.5 mA, 1-s duration) were randomly delivered with inter-trial intervals of 120 s. Shock delivery onset was used as the trigger event for data alignment.

**Real-time animal detection and closed-loop optogenetic control**

Customized software was used for online real-time animal detection (Python 3.4, <http://www.python.org/> with OpenCV library, <https://opencv.org/>).<sup>108</sup> The behavior of the animal was monitored using an infrared camera at 24fps. Each frame was gaussian blurred and then binarized. The gravity center for the detected contour was used to determine the location of the animal. In the two-chamber place preference test, the stimulation chamber was randomly assigned (balanced within the group) to each animal. Once the mouse entered the stimulation chamber, a computer-controlled Arduino microcontroller (<https://www.arduino.cc/>) would generate TTL signals to drive the LED light source (ThorLabs Inc.). The behavior test was run automatically without experimenter's interference and the result was calculated right after each experiment.

**RNAscope assay**

RNAscope hybridization was performed using the RNAscope Multiplex Fluorescent Reagent Kit v2 Assay (ACD). The assay was performed according to its manufacturer's instructions. The staining procedures were similar as we previously described.<sup>109</sup> Briefly, wild-type mice were transcardially perfused, and the brains were removed and post-fixed in 4% paraformaldehyde (PFA) for 24 h at 4°C. Then the brain tissue was dehydrated sequentially in 20% and 30% sucrose. Coronal brain sections were cut at 40 µm using a cryostat (CM3050S, Leica). Collected sections were mounted on slides and baked for 30 min at 60°C and post-fixed in 4% PFA for 15 min at 4°C. Then, the sections were dehydrated in increasing ethanol concentrations (50%, 70% and 100%), followed by incubation of Hydrogen Peroxide for 10 min at room temperature (RT). Next, target retrieval was made by immersing the slides into double distilled (dd) H<sub>2</sub>O for 10-s and into Retrieval Reagent for 5 min at 99°C in a humidity saturated environment. The slides were cooled in dd H<sub>2</sub>O for 15-s, then transferred to 100% alcohol for 3 min at RT. Then, the sections were incubated in Protease III for 30 min at 40°C, followed by wash with dd H<sub>2</sub>O. The sections were incubated with RNAscope probes—Mm-Slc17a6 (Vglut2), Mm-Slc32a1-C2 (Vgat) for 2 h at 40°C, followed by amplifying hybridization processes (AMP1 and AMP2 for 30 min; AMP3 for 15 min). Finally, the HRP probes (HRP-C1, HRP-C2) were hybridized for 15 min at 40°C, followed by 30 min incubation with Opal fluorescent ligands (Opal 570, and Opal 690, 1:1500 dilution) for 30 min at 40°C sequentially. The HRP blocker was applied for 15 min at 40°C between each HRP probe hybridization. Finally, the sections were counterstained with DAPI for 30 s at RT, before placing the coverslips. Fluorescence images were acquired using a confocal microscope with a 10× objective.

**Slice recording**

To examine the connectivity between PCG GABAergic and glutamatergic neurons, Vgat-Cre::Ai14 mice injected with AAV1-EF1 $\alpha$ -DIO-hChR2 (H134R)-EYFP-WPRE in PCG were used for slice recording. To confirm the connectivity between PCG axons and VTA GABAergic neurons, Vgat-Cre::Ai14 mice injected with AAV1-hSyn-hChR2 (H134R)-EYFP in PCG were used for slice recording. After three weeks injections, the *in vitro* acute brain slice recording was performed. Animals were anesthetized by urethane and then decapitated and the brain was rapidly removed and immersed in an ice-cold dissection buffer (composition: 60 mM NaCl, 3 mM KCl, 1.25 mM NaH<sub>2</sub>PO<sub>4</sub>, 25 mM NaHCO<sub>3</sub>, 115 mM sucrose, 10 mM glucose, 7 mM MgCl<sub>2</sub>, 0.5 mM CaCl<sub>2</sub>; saturated with 95% O<sub>2</sub> and 5% CO<sub>2</sub>; pH = 7.4). The brain slices were coronally sectioned into 300-µm-thick sections with a vibratome (Leica VT1000s). Slices were allowed to recover for 30 min in a submersion chamber filled with the warmed (35 °C) ACSF (composition, 119 mM NaCl, 26.2 mM NaHCO<sub>3</sub>, 11 mM glucose, 2.5 mM KCl, 2 mM CaCl<sub>2</sub>, 2 mM MgCl<sub>2</sub>, 1.2 mM NaH<sub>2</sub>PO<sub>4</sub>, 2 mM sodium pyruvate, 0.5 mM VC).

PCG neurons labeled with tdTomato (Vgat-Cre-tdTomato mice), VTA GABAergic neurons labeled with tdTomato (Vgat-Cre-tdTomato mice) or surrounded by EYFP+ fibers were visualized under a fluorescence microscope (Olympus BX51 WI). Patch pipettes (resistance of ~4–5 MΩ) filled with a cesium-based internal solution (composition, 125 mM cesium gluconate, 5 mM TEA-Cl, 2 mM NaCl, 2 mM CsCl, 10 mM HEPES, 10 mM EGTA, 4 mM ATP, 0.3 mM GTP and 10 mM phosphocreatine, pH 7.25; 290 mOsm) were used for whole-cell recordings. Signals were recorded with an Axopatch 700B amplifier (Molecular Devices) under voltage-clamp mode at a holding voltage of -70 mV for excitatory currents, filtered at 2 kHz and sampled at 10 kHz. Tetrodotoxin (TTX, 1 µM) and 4-aminopyridine (4-AP) (1 mM) were added to the external solution for recording monosynaptic responses to blue light stimulation (5-ms pulse, power of 3 mW, 10–30 trials).

**Histology, imaging, and quantification**

Following all experiments, the animals were deeply anesthetized under isoflurane and perfused transcardially with phosphate-buffered saline (PBS) followed by 4% PFA. The brain was removed and post-fixed with 4% PFA for 24 h at 4°C. It was coronally sectioned into 150-µm-thick sections with a vibratome (Leica Microsystems). The free-floating sections were first washed three times with PBS for 10 min each time. The sections were then stained with Nissl reagent (Deep red, Invitrogen) for 3 h at room temperature. Aluminum foil was used to shield the sections from light. All the slices were examined under a confocal microscope (Olympus FluoView FV1000). To quantify the relative density of axonal projections of PCG neurons in downstream structures, brain regions of interest were collected and imaged and scanned at 10× magnification with the same parameters (such as laser power, scan speed, auto gain and offset value). Fluorescence quantifications were performed using FIJI (ImageJ. 2.1.0, NIH) by converting the images into monochromatic. Intensity value of the interest brain regions (200 × 200 pixel) were normalized to the baseline value. Four sections were collected and averaged for each of brain structures. The fluorescence density for each target structure was normalized for each animal and averaged across the animal group.

**QUANTIFICATION AND STATISTICAL ANALYSIS****Data analysis**

For multichannel optrode recordings, spike trains were sorted offline. The signals were filtered through a bandpass filter (0.3–3 kHz). The 16-channel probes were grouped into four tetrodes and then performed semiautomatic spike sorting by using Offline Sorter (Plexon) following our previous studies.<sup>38,104</sup> To identify the units driven directly by ChR2 activation, we analyzed the onset latency of spikes relative to the onset of light stimulation. Only spikes with latency < 3-ms were considered as being directly stimulated in this study. The average waveforms were computed and compared between LED-evoked and sensory-evoked spikes. For noise and air puff response quantification, the Z score was calculated as the firing rate (calculated within a 100-ms window after the stimulus onset)

divided by the standard deviation of the baseline firing rate (calculated within a 50-ms window before the stimulus onset), with 1-ms bin. For sucrose response quantification, firing rates were normalized to the baseline activity by calculating a Z score, with 10-ms bin,<sup>10</sup> and for each cell, the evoked response within 2 s after the stimulus onset was compared.

### Statistics

Shapiro–Wilk test was first used to examine whether samples had a normal distribution. In the case of a normal distribution, parametric tests were used. For two group comparison, significance was determined by using Student's t test. Paired t test was used to compare data from the same neuron or the same animal. One-way ANOVA followed by LSD or Tukey post hoc comparison was used for multiple comparisons. Significance level was marked as \*:  $p < 0.05$ ; \*\*:  $p < 0.01$ ; and \*\*\*:  $p < 0.001$ . Data are presented as mean  $\pm$  SD, unless otherwise indicated. Statistical analysis was conducted using SPSS (IBM).